Dalton Transactions

MnIII-Peroxo Adduct Supported by a New Tetradentate Ligand Shows Acid-Sensitive Aldehyde Deformylation Reactivity

Journal:	*Dalton Transactions*
Manuscript ID	DT-ART-06-2018-002300.R1
Article Type:	Paper
Date Submitted by the Author:	23-Aug-2018
Complete List of Authors:	Denler, Melissa; University of Kansas, Chemistry Wijeratne, Gayan; University of Kansas, Chemistry Derek, Rice; University of Kansas, Chemistry Colmer, Hannah; University of Kansas, Chemistry Day, Victor; University of Kansas, Chemistry Jackson, Timothy; University of Kansas, Chemistry

Mn^{III}-Peroxo Adduct Supported by a New Tetradentate Ligand Shows Acid-Sensitive Aldehyde Deformylation Reactivity

Melissa C. Denler,[‡a] Gayan B. Wijeratne,[‡a,b] Derek B. Rice,[a] Hannah E. Colmer,[a,c] Victor W. Day,[a] Timothy A. Jackson*[a]

[a]*The University of Kansas, Department of Chemistry and Center for Environmentally Beneficial Catalysis, 1251 Wescoe Hall Drive, Lawrence, KS 66045, USA.*

[b]*Current address: The University of Alabama at Birmingham, Department of Chemistry, Center for Biophysical Sciences and Engineering, 1025 18th Street South, Birmingham AL 35205*

[c]*Current address: University of Saint Mary, 4100 S 4th Street, Leavenworth, KS 66048, USA.*
[*]*Corresponding author*

† Electronic supplementary information (ESI) available: Crystal data and structure refinement, NMR data for ligand and organic substrates, additional spectroscopic data for Mn intermediates, DFT-optimized cartesian coordinates, TD-DFT-calculated spectra. CCDC 1844299. For ESI and crystallographic data in CIF or other electronic format see DOI: XXX

‡ The contributions of these authors were of equal merit.

*To whom correspondence should be addressed:
Timothy A. Jackson
Phone: (785) 864-3968
email: taj@ku.edu

Abstract: The new tetradentate L^7BQ ligand (L^7BQ = 1,4-di(quinoline-8-yl)-1,4-diazepane) has been synthesized and shown to support Mn^{II} and Mn^{III}-peroxo complexes. X-ray crystallography of the $[Mn^{II}(L^7BQ)(OTf)_2]$ complex shows a monomeric Mn^{II} center with the L^7BQ ligand providing four donor nitrogen atoms in the equatorial field, with two triflate ions bound in the axial positions. When this species is treated with H_2O_2 and Et_3N at -40 °C, a Mn^{III}-peroxo adduct, $[Mn^{III}(O_2)(L^7BQ)]^+$ is formed. The formation of this new intermediate is supported by a variety of spectroscopic techniques, including electronic absorption, Mn K-edge X-ray absorption and electron paramagnetic resonance methods. Evaluation of extended X-ray absorption fine structure data for $[Mn^{III}(O_2)(L^7BQ)]^+$ resolved Mn–O bond distances of 1.85 Å, which are on the short end of those previously reported for crystallographically characterized Mn^{III}-peroxo adducts. An analysis of the X-ray pre-edge region of $[Mn^{III}(O_2)(L^7BQ)]^+$ revealed a large pre-edge area of 20.8 units. Time-dependent density functional theory computations indicate that the pre-edge intensity is due to Mn 4p-3d mixing caused by geometric distortions from centrosymmetry induced by both the peroxo and L^7BQ ligands. The reactivity of $[Mn^{III}(O_2)(L^7BQ)]^+$ towards aldehydes was assessed through reaction with cyclohexanecarboxaldehyde and 2-phenylpropionaldehyde. From these experiments, it was determined that $[Mn^{III}(O_2)(L^7BQ)]^+$ only reacts with aldehydes in the presence of acid. Specifically, the addition of cyclohexanecarboxylic acid to $[Mn^{III}(O_2)(L^7BQ)]^+$ converts the Mn^{III}-peroxo adduct to a new intermediate that could be responsible for the observed aldehyde deformylation activity. These observations underscore the challenges in identifying the reactive metal species in aldehyde deformylation reactions.

Introduction

Peroxomanganese(III) adducts have been proposed as intermediates for several manganese-dependent enzymes, including manganese superoxide dismutase,[1-2] manganese dioxygenase,[3-4] oxalate oxidase[5-6] and oxalate decarboxylase.[7-8] Peroxo-level intermediates have also been proposed for the dinuclear enzymes manganese catalase[9] and the manganese-dependent version of ribonucleotide reductase (Mn-RNR).[10-11] Mechanistic understanding for a majority of these enzymes is incomplete, which warrants detailed studies of synthetic model systems. To this end, small molecule model complexes have long served as useful tools in understanding the mechanisms of metalloenzymes.[12-14] In addition to these biological motivations, a better understanding of the structure and reactivity of peroxomanganese(III) intermediates is also of relevance for synthetic manganese catalysts used in substrate oxidation reactions.[15-21]

Solid-state X-ray diffraction structures have been reported for several peroxo-manganese species, including both side-on (η^2) peroxomanganese(III) adducts,[22-28] and end-on (η^1) alkylperoxomanganese(III) adducts.[29-30] Apart from these, the majority of peroxomanganese(III) species have been observed under cryogenic conditions and have been thoroughly characterized using a combination of spectroscopic and computational methods.[31-41] Complementary investigations of the chemical reactivity of peroxomanganese(III) complexes have revealed several modes of reactivity, including common decay pathways (such as the formation of dimers), which are summarized in Scheme 1.

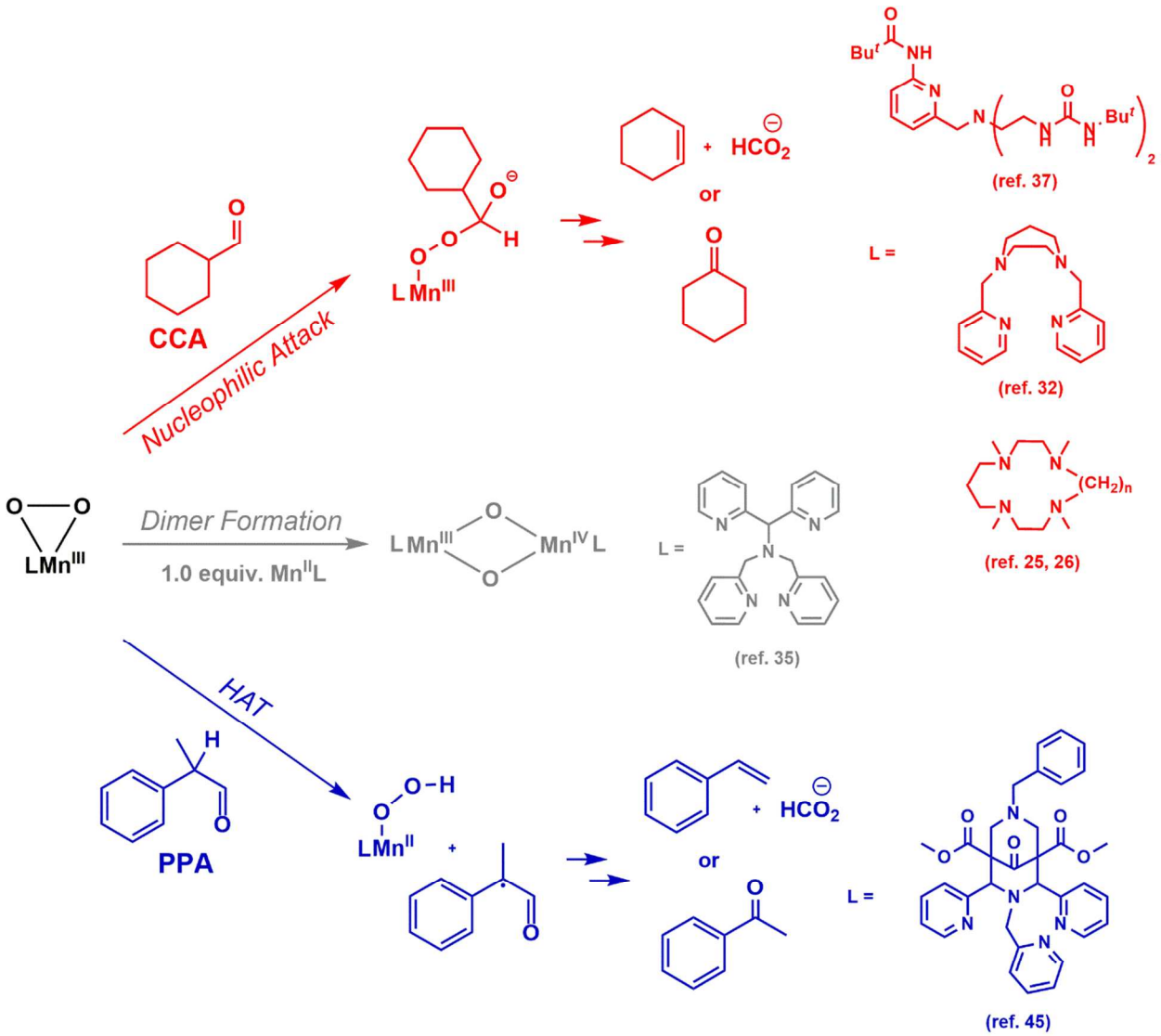

Scheme 1. Common reactions for peroxomanganese(III) complexes.

The ability of peroxomanganese(III) complexes to perform aldehyde deformylation has been known for some time.[42] There are several reports of Mn^{III}-peroxo adducts that deformylate cyclohexanecarboxaldehyde (CCA; see Scheme 1, top), although the mechanism for deformylation is not fully understood.[25-26, 32, 34, 37] Support for nucleophilic attack of the peroxo ligand on the aldehyde carbonyl carbon comes from kinetic studies that showed faster decay of Mn^{III}-peroxo adducts in the presence of electron-poor, *para*-substituted benzaldehydes. Hammett analyses of these systems yielded ρ^+ values from +1.5 to +2.5.[26, 32]

The nucleophilicity of Mn^{III}-peroxo adducts is likely also responsible for a commonly identified decay pathway, where the Mn^{III}-peroxo unit attacks unreacted Mn^{II} complex to form oxo-bridged $Mn^{III}Mn^{IV}$ product (Scheme 1, center). For example, the peroxomanganese(III) complex, $[Mn^{III}(O_2)(\kappa^4\text{-N4py})]^+$ (where N4py is the neutral N_5 ligand *N*,*N*-bis(2-pyridylmethyl)-*N*-bis(2-pyridyl)methylamine) was observed to convert to a bis(μ-oxo)dimanganese(III,IV) complex upon addition of $[Mn^{II}(N4py)(OTf)]^+$.[35] More recently, we have reported spectroscopic studies of the reaction of $[Mn^{III}(O_2)(Me_2EBC)]^{2+}$ (where Me_2EBC is the cross-clamped macrocyclic ligand 4,11-dimethyl-1,4,8,11-tetraazabicyclo[6.6.2]-hexadecane) with $[Mn^{II}(Cl)_2(Me_2EBC)]$, which provided evidence for the formation of a mixture of mononuclear Mn^{IV} and Mn^{III} products.[43] Both of these reactions are presumed to proceed through a μ-peroxodimanganese(II,III) intermediate. Quite recently, McDonald and co-workers have provided spectroscopic evidence for a μ-peroxodimanganese(II,III) species supported by the dinucleating ligand HPTB (HPTB = *N*,*N*,*N*′,*N*′-tetrakis(2-(benzimidazolyl))-2-hydroxy-1,3-diaminopropane).[44]

In contrast to these modes of reactivity that rely on the nucleophilicity of the Mn^{III}-peroxo unit, there are several examples of peroxomanganese(III) adducts acting as hydrogen-atom acceptors (Scheme 1, bottom). Borovik and co-workers showed that a peroxomanganese(III) adduct supported by a tripodal ligand with a hydrogen-bonding cavity forms a hybrid Mn^{III}-oxo/hydroxo species after reaction with the hydrogen-atom donor diphenylhydrazine.[37] More recently, Sastri and co-workers showed that a Mn^{III}-peroxo supported by an aminopyridyl ligand effects the deformylation of 2-phenylpropionaldehyde (PPA) by a hydrogen-atom transfer mechanism.[45] This alternate mechanism for deformylation was supported by the observation of

an H/D kinetic isotope effect when the benzylic C–H bond of PPA was substituted for deuterium.

The ability of the Mn^{III}-peroxo unit to abstract hydrogen atoms from benzylic C–H bonds, such as those of PPA, offers a new perspective on the decay pathways of Mn^{III}-peroxo adducts supported by aminopyridyl ligands. This includes the decay reaction of the $[Mn^{III}(O_2)(MeTPEN)]^+$ complex (where MeTPEN is *N*-methyl-*N*,*N*′,*N*′-tris(2-pyridylmethyl)ethane-1,2-diamine; see Scheme 2),[41] which resulted in the eventual formation of a Mn^{II} complex coordinated by two pyridinecarboxylate ligands (Scheme 2) derived from the oxidation of the parent MeTPEN ligand. Anxolabéhère-Mallart and co-workers postulated that this decay pathway, which required the addition of strong acid, proceeded through a Mn^{III}-hydroperoxo species that underwent O–O cleavage to afford a strong oxidant (i.e., a high-valent Mn^{IV}-oxo adduct) capable of initiating oxidation of the MeTPEN ligand at the benzylic linkers.[41] In light of the more recent studies that suggest that Mn^{III}-peroxo and Mn^{III}-hydroperoxo adducts can attack benzylic C–H bonds, it is unclear if it is necessary to invoke formation of a high-valent manganese-oxo species to rationalize the observed chemistry.

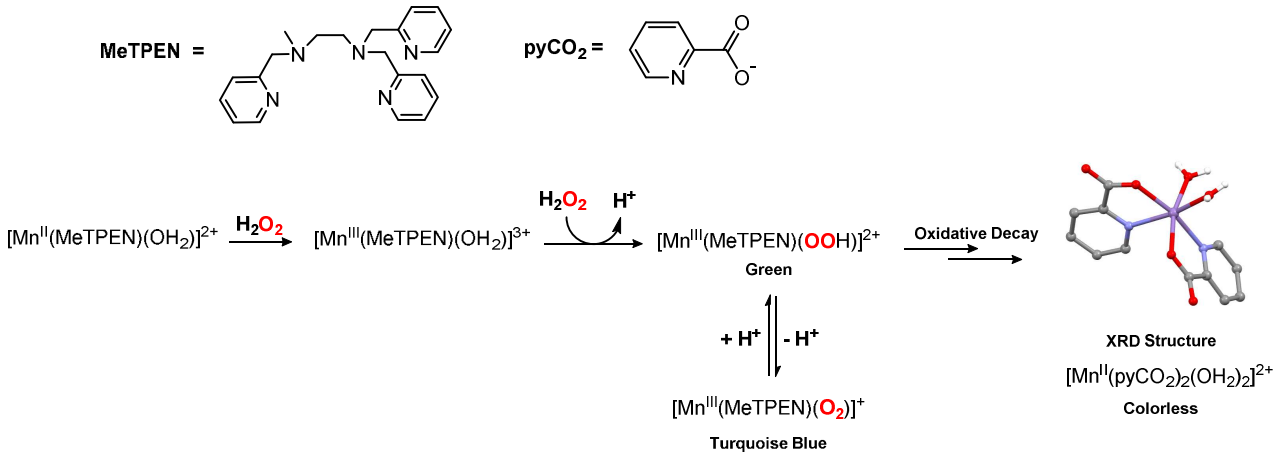

Scheme 2. The proposed formation and ligand oxidation pathway of a Mn^{III}-peroxo and Mn^{III}-hydroperoxo species supported by the *N*-methyl-*N*,*N*′,*N*′-tris(2-pyridylmethyl)ethane-1,2-diamine ligand (MeTPEN). The XRD structure, taken from reference 41, shows the final manganese

decay product in the presence of acid, where the metal center is coordinated to two pyridine carboxylate molecules ($pyCO_2^-$) that resulted from ligand oxidation.

Because of the potential for Mn^{III}-peroxo and Mn^{III}-hydroperoxo adducts to attack C–H bonds of moderate strength (ca. 80 – 85 kcal/mol), the design and synthesis of a novel ligand platform excluding benzylic $–CH_2$ linkers is of interest, as this ligand could avoid hydrogen atom abstraction as a decay pathway. To develop such a ligand, we chose a ligand topology quite similar to that of the $L^7py_2^R$ family that we had previously used to generate a series of Mn^{III}-peroxo adducts (Figure 1).[31-32, 34] In this study, we report the synthesis of the L^7BQ ligand (L^7BQ = 1,4-di(quinolin-8-yl)-1,4-diazepane), which lacks benzylic linkers, and describe the corresponding Mn^{II} complex, $[Mn^{II}(L^7BQ)(OTf)_2]$. As anticipated, the $[Mn^{II}(L^7BQ)(OTf)_2]$ complex reacts with H_2O_2 and Et_3N to generate the peroxomanganese(III) complex, $[Mn^{III}(O_2)(L^7BQ)]^+$, which has been characterized by a variety of spectroscopic techniques. Although the $[Mn^{III}(O_2)(L^7BQ)]^+$ complex does not show enhanced stability relative to the $[Mn^{III}(O_2)(L^7py_2^R)]^+$ analogues, the reactivity of this complex with respect to aldehydes is distinct and highly sensitive to the presence of acid, suggesting a ligand influence on reactivity.

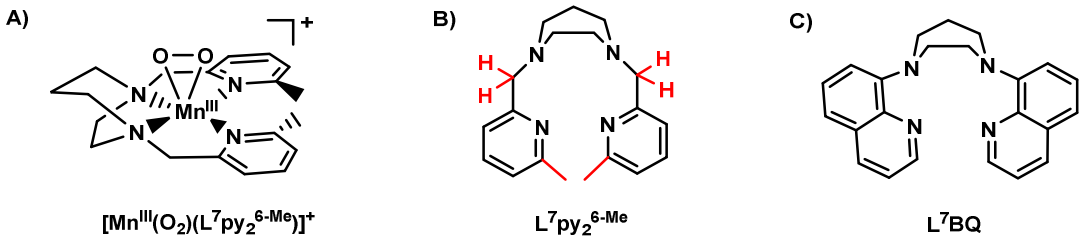

Figure 1. The schematic structures of A) $[Mn^{III}(O_2)(L^7py_2^{6\text{-}Me})]^+$ B) $L^7py_2^{6\text{-}Me}$ ligand (with benzylic groups potentially susceptible to oxidation highlighted in red), and C) the new L^7BQ ligand described in this work.

Experimental Methods

Materials. Unless otherwise noted, all chemicals and solvents were obtained from commercial vendors at ACS grade or better and were used without further purification. Acetonitrile, methanol, and ether were dried and degassed using a Pure Solv (2010) solvent purification system. Toluene was made anaerobic by either sparging and then drying over activated alumina using a PPT Glass Contour solvent purification system, or dry toluene (99% purity) from Acros Organics was degassed by four freeze-pump-thaw cycles using Schlenk techniques. All dried, degassed solvents were immediately taken into an argon-filled glove box and were stored in tightly-sealed Schlenk glassware until use. CCA was distilled prior to use; however, a ^{1}H-NMR analysis of the material following distillation revealed the persistence of acid impurities (*vide infra*). Syntheses of $L^{7}BQ$ and $[Mn^{II}(L^{7}BQ)(OTf)_2]$ were carried out under inert conditions, as described below. Product analysis was performed by running reaction mixtures through a silica plug with excess EtOAc, and 1,2,4,5-tetrachloro-3-nitrobenzene was used as an internal standard for ^{1}H NMR quantification.

Instrumentation. NMR spectra were collected on a Bruker DRX 400 MHz spectrometer and a 600 MHz AVAN CE III spectrometer with a BBO probe or a QNP probe. Data were collected at room temperature in $CDCl_3$ (δ = 7.26 ppm), unless stated otherwise. Mass spectrometry experiments were performed using an LCT Primers MicroMass electrospray time-of-flight instrument. Electronic absorption spectra were obtained on a Varian Cary 50 Bio spectrophotometer interfaced with a Unisoku cryostat (USP-203-A) capable of maintaining temperatures between 150 and 373 K. EPR spectra were collected on an X-band (9 GHz) Bruker EMXPlus spectrometer equipped with an Oxford ESR900 continuous flow liquid helium cryostat and an Oxford ITC503 temperature system. Both parallel- and perpendicular-mode spectra were collected using a Bruker ER4116DM dual-mode cavity. All spectra were collected under

nonsaturating conditions at 2.0 mW microwave power, 4 G modulation amplitude, 100 kHz modulation frequency and 83 ms time constant. Spin quantification of the product of $[Mn^{III}(O_2)(L^7BQ)]^+$ with cyclohexanecarboxylic acid (termed intermediate A) was determined against a 2.5 mM sample of $[Mn^{II}(L^7BQ)(OTf)_2]$ in MeCN. Gas chromatography-mass spectrometry data were collected using a Quattro Micro GC quadrupole mass analyzer via an Agilent 6890 N gas chromatograph. A 5% phenyl methyl silicone stationary phase (HP-5 MS) 12 meter column was used along with a helium carrier gas at a flow rate of 2 ml min^{-1}. The injector port was heated to 240 □C and 1 μL of sample was injected with a split ratio of 20:1. The GC thermal gradient was an initial 50 □C, which was held for 1 minute before increasing 50 □C min^{-1} to 300 □C and held for two minutes. Elemental analysis was done through Micro-Analysis, Inc.

Synthesis of the L^7BQ Ligand. 8-bromoquinoline (500 mg, 2.4 mmol), homopiperazine (120 mg, 1.2 mmol), and NaO^tBu (324 mg, 3.4 mmol) were combined in a Schlenk tube in dry, degassed toluene (40 mL), along with 4 mol% $Pd_2(dba)_3$ (110 mg, 0.12 mmol), and 10 mol% BINAP (150 mg, 0.24 mmol) within an argon-filled glove box. The tube was sealed with an air-tight septum, and stirred at 110 ^oC for three days. Although no difficulties were encountered, heating a sealed vessel can result in explosion of the reaction vessel. Because of this, all reactions were performed behind a blast shield. After heating for three days, the reaction mixture was cooled to room temperature and was diluted with excess diethyl ether. This mixture was filtered through celite and evaporated to dryness under reduced pressure. The crude product was purified by flash chromatography over silica gel using ethyl acetate and hexane (1 : 20) as the beginning eluent and the percentage of ethyl acetate was gradually increased over time. The clean ligand was isolated as a yellow oil in 69% yield (292 mg) and was characterized by ^1H

NMR, ^{13}C NMR, HSQC and ESI-MS. ^{1}H NMR data (600 MHz, Figure S1) for L^7BQ ($CDCl_3$, δ) = 8.86 (dd, *J* = 4.1, 1.9 Hz, 2H), 8.09 (dd, *J* = 8.3, 1.9 Hz, 2H), 7.40 (t, *J* = 7.8 Hz, 2H), 7.35 (dd, *J* = 8.2, 4.1 Hz, 2H), 7.31 (dd, *J* = 8.2, 1.3 Hz, 2H), 7.21 (dd, *J* = 7.6, 1.4 Hz, 2H), 4.09 (s, 4H), 3.96 – 3.76 (m, 4H), 2.38 (p, *J* = 5.7 Hz, 2H). ^{13}C NMR data (400 MHz, Figure S2) for L^7BQ ($CDCl_3$, δ) = 149.85, 147.39, 142.61, 136.43, 130.03, 126.82, 120.81, 119.64, 115.61, 55.16, 53.55, 29.06. HSQC for L7BQ in included in the supporting information (Figure S3). ESI-MS (Figure S4): $[L^7BQ + H]^+$ *m/z* = 355.1902 (calc. = 355.1917).

Synthesis of $[Mn^{II}(L^7BQ)(OTf)_2]$. An equimolar mixture of L^7BQ and $[Mn^{II}(OTf)_2(MeCN)_2]_n$ produced high yields (>90%) of $[Mn^{II}(L^7BQ)(OTf)_2]$ when stirred overnight in MeCN under an inert atmosphere at room temperature. $[Mn^{II}(OTf)_2(MeCN)_2]_n$ was synthesized according to literature procedures.[25] A detailed procedure for the metalation of L^7BQ is as follows. To a stirred MeCN solution (5 mL) of L^7BQ (100 mg, 0.282 mmol), an equimolar quantity of $Mn^{II}(OTf)_2$ (99 mg, 0.282 mmol) was added in the same solvent (5 mL) and was stirred overnight under an inert atmosphere. The mixture was then filtered using a syringe filter and dried under reduced pressure. The solid product was recrystallized with MeCN and Et_2O by vapor diffusion. Light yellow crystals suitable for X-ray diffraction analysis were obtained by subsequent recrystallization with the same solvent system. $[Mn^{II}(L^7BQ)(OTf)_2]$ was further characterized by the effective magnetic moment analysis by the ^{1}H NMR method of Evans[46] in CD_3CN at 25 ^{o}C, and by ESI-MS and EPR methods. The effective magnetic moment of $[Mn^{II}(L^7BQ)(OTf)_2]$ at 25 ^{o}C was found to be 5.7 μ_B in CD_3CN (a diamagnetic correction, χ_D, of -277.24 x 10^{-6} emu mol^{-1} was included in the calculation of the molar magnetic susceptibility, χ_M).[47] This value agrees with the expected value (5.9 μ_B) for a monomeric high-spin Mn^{II} center. ESI-MS (Figure S5): $[Mn^{II}(L^7BQ)(OTf)]^+$ *m/z* = 558.0342 (calc. = 558.0745). The

perpendicular-mode X-band EPR spectrum of a frozen MeCN solution of $[Mn^{II}(L^7BQ)(OTf)_2]$ exhibits features at 230 mT and 350 mT at 5 K (Figure S6, left), which are characteristic of a monomeric Mn^{II} species.[35] Additionally, the parallel-mode EPR spectrum shows no signal (Figure S6, right). Elemental Analysis $[Mn^{II}(L^7BQ)(OTf)_2]\cdot H_2O$ $C_{25}H_{24}F_6MnN_4O_7S_2$ calc (%): C 41.38, H 3.33, N:7.72; Found (%): C 41.60, H: 3.23, N: 7.73.

X-ray diffraction data collection and analysis for $[Mn^{II}(L^7BQ)(OTf)_2]$. A light-yellow single-domain crystal of $[Mn^{II}(L^7BQ)(OTf)_2]$ was suspended with Paratone N oil on a MiteGen MicroMount and placed on a goniometer head in a cold nitrogen stream at 100 K for a single-crystal X-ray structure determination. Monochromatic X-rays were provided by a Bruker diffractometer equipped with Helios multilayer optics, an APEX II CCD detector, and a Bruker MicroStar microfocus rotating anode X-ray source operating at 45 kV and 60 mA. Intensity data (5238 0.5°-wide ω- or φ-scan frames with counting times of 2-3 seconds each) were collected with the Bruker program SMART,[48] and diffracted intensities were measured with the Bruker program SAINT.[49] The space group[50] and crystallographic data are summarized in Table S1. The Bruker software package SHELXTL was used to solve the structure and locate all nonhydrogen atoms with "direct methods" techniques. Hydrogen atoms were located from a difference Fourier and included in the structural model as independent isotropic atoms whose parameters were allowed to vary in least-squares refinement cycles. All stages of weighted full-matrix least-squares refinement were conducted using F_o^2 data with the SHELXTL Version 2010.3-0 software package.[51] The final structural model incorporated anisotropic thermal parameters for all non-hydrogen atoms and isotropic thermal parameters for all hydrogen atoms.

Generation and Characterization of $[Mn^{III}(O_2)(L^7BQ)]^+$. The peroxomanganese(III) complex $[Mn^{III}(O_2)(L^7BQ)]^+$ was generated by treating a 2.5 mM MeCN solution of

$[Mn^{II}(L^7BQ)(OTf)_2]$ with 5 equiv. H_2O_2 and 1.0 equiv. Et_3N at -40 ^oC. Reactions using less than 5 equiv. hydrogen peroxide resulted in substantially lower formation of the Mn^{III}-peroxo adduct. We presume that water, which is added with the H_2O_2, is a strong enough base to remove the second proton required for formation of the side-on peroxomanganese(III) species. When greater equiv. Et_3N were used, we observed the decay of $[Mn^{III}(O_2)(L^7BQ)]^+$ to be more rapid. One equiv. Et_3N gave the cleanest formation and the best thermal stability.

Because this species was sensitive to the temperature of the added reagents, syringes and stock solutions were chilled prior to addition in order to minimize any thermal decay. Additionally, the stock solutions were re-made often to avoid the base-catalyzed decomposition of hydrogen peroxide.[52] Characteristic changes in the electronic absorption spectrum were evident of the formation of $[Mn^{III}(O_2)(L^7BQ)]^+$, where the growth of two bands at 450 nm (ε = 260 M^{-1} cm^{-1}) and 660 nm (ε = 75 M^{-1} cm^{-1}) marked the formation of this species. ESI-MS $[Mn^{III}(O_2)(L^7BQ)]^+$ *m/z* = 441.1135 (calc. = 441.1123 *m/z*); $[Mn^{III}(^{18}O_2)(L^7BQ)]^+$ *m/z* = 445.1156 (calc. = 445.1208 *m/z*) (Figures S7 and S8). EPR samples of $[Mn^{III}(O_2)(L^7BQ)]^+$ were prepared at -40 ^oC in MeCN using cryogenic techniques and were analyzed at 5 K (Figure S9). Attempts to characterize $[Mn^{III}(O_2)(L^7BQ)]^+$ by vibrational methods were unsuccessful. We note that, to date, vibrational studies of side-on Mn^{III}-peroxo adducts have commonly been unsuccessful.[35, 40]

XAS Sample Preparation. Frozen solution samples of $[Mn^{II}(L^7BQ)(OTf)_2]$ at 11 mM and $[Mn^{III}(O_2)(L^7BQ)]^+$ at 2.5 mM were prepared from 400 μL of solution in MeCN that was frozen in a precooled sample cup. A frozen solution sample of the product of $[Mn^{III}(O_2)(L^7BQ)]^+$ with cyclohexanecarboxylic acid (termed intermediate A) was prepared from 400μL of a 2.5 mM solution in MeCN that was frozen in a precooled sample cup following the addition of cyclohexanecarboxylic acid to $[Mn^{III}(O_2)(L^7BQ)]^+$.

Product Analysis GC-MS was used for analysis of organic products from the reactions of Mn complexes with aldehydes, and the percent yield of these reactions was determined by comparing the ratio of the product signal to that of an internal standard and comparing the ratio to a standard curve for the product. A detailed procedure is a follows: a 2.5 mM solution of $[Mn^{III}(O_2)(L^7BQ)]^+$ was reacted with 165 equivalents of CCA at −40 °C in MeCN. When the reaction was completed, it was allowed to warm to room temperature, napthalene was added as an internal standard, and the reaction solution was run through a silica plug with excess EtOAc. The reaction was performed in triplicate. The work-up procedure was tested using a standard sample of known substrate and product concentrations, and the procedure was not found to change the substrate:product ratio.

XAS Data Collection. The Mn K-edge XAS data for all samples were collected over an energy range of 6300 to 7250 eV. Under all conditions, a manganese foil was used as reference for each scan by assigning the zero crossing of the second derivative of the K-edge energy of the foil to 6539.0 eV. All XAS data were obtained via fluorescence excitation. Data for $[Mn^{III}(O_2)(L^7BQ)]^+$ and the product of $[Mn^{III}(O_2)(L^7BQ)]^+$ with cyclohexanecarboxylic acid (termed intermediate A) were collected at beamline 9-3 at SSRL at 7 K using a Si(220) monochromator and a 100-element Ge array detector. Data for $[Mn^{II}(L^7BQ)(OTf)_2]$ were collected at beamline X3B at the National Synchrotron Light Source (NSLS) using a Si(111) monochromator and a 31-element Ge array detector.

XAS Data Analysis. Processing of the XAS data for $[Mn^{II}(L^7BQ)(OTf)_2]$ was done using EXAFSPAK[53] using previously described methods.[43] Analysis of EXAFS data for $[Mn^{III}(O_2)(L^7BQ)]^+$ and intermediate A were performed using *DEMETER*.[54] The *AUTOBK* algorithm, as implemented in *ATHENA*, was used for background removal. The edge-step

normalization procedure was used for each data set. EXAFS refinement in *ARTEMIS* was carried out on $k^3\chi(k)$ data, using phase and amplitude functions obtained from *FEFF*, version 6,[55] and a structural model of $[Mn^{III}(O_2)(L^7BQ)]^+$ from DFT computations. For each fit, the parameters *r* (average distance between Mn and scattering atom), E_0 (a single value for all paths), and σ^2 (Debye-Waller factor) were optimized, while *n*, the number of atoms in the shell, was kept fixed. *n* was varied by integer steps systematically to achieve better goodness of fit. The goodness of fit was evaluated using the R-factor:

$$R = \sum_{i=1}^{N}(\chi_i^{data} - \chi_i^{fit})^2 \,/\, \sum_{i=1}^{N}(\chi_i^{data})^2$$

Fits of the pre-edge area were performed using the FityK software.[56] Pre-edge intensity was normalized relative to the most intense fluorescence peak. The pre-edge was fit using pseudo-Voight line shapes and varied full-width at half-maximum, energy position, and height. The contribution from the rising edge and the background were also fit using a pseudo-Voight function. Manganese K-edge energy values were determined based on the position of the inflection point of the rising edge upon taking the first derivative of the edge region.

Density Functional Theory. All calculations were performed using the *ORCA* 4.0 software package.[57] Geometries for $[Mn^{III}(O_2)(L^7BQ)]^+$ were performed starting from the Mn^{II} crystal structure and adding the peroxo moiety. The high-spin $S = 2$ spin state was used for all computations. Optimizations were carried out using the B3LYP functional with the inclusion of dispersion interactions via Grimme's D3 correction with the Becke-Johnson damping scheme.[58-61] The def2-TZVP basis set was utilized for Mn, N, and O and the def2-SVP basis set was used for C and H.[62-63] A larger DFT integration grid, Grid6 in ORCA nomenclature, was utilized. The RIJCOSX approximation was used with a larger COSX grid (GridX6) and the def2/J auxiliary basis sets. Solvent was included implicitly through the SMD solvation model with the default

parameters in ORCA for acetonitrile.[64] Structures were confirmed to be a minima through numerical frequency calculations performed at the same level of theory.

The manganese pre-K-edge spectra of $[Mn^{III}(O_2)(L^7BQ)]^+$ models were calculated using time-dependent density functional theory (TD-DFT) within the Tamm-Dancoff approximation using the B3LYP functional.[65-66] Calculations were performed using the zeroth-order approximation (ZORA) with the ZORA-def2-TZVP(-f) basis sets used for all atoms.[67-68] The pre-edge area was calculated using a previously published method based on calibration using a series of Mn^{II} and Mn^{III} complexes, where the origin adjusted intensity (I) is calculated from the sum of the electric dipole, electric quadrupole, and magnetic dipole contributions. These values are used in the empirically derived equation $A = 6.01I + 1.79$ for B3LYP.[69] Simulations of the spectra were performed with a 1 eV linewidth.

The electronic absorption spectra of $[Mn^{III}(O_2)(L^7BQ)]^+$ models were calculated using TD-DFT methods utilizing the B3LYP functional. The def2-TZVPP basis set was used for Mn, N, and O and the def2-TZVP basis set for C and H. Solvation was included implicitly using the SMD solvation model with the default values for acetonitrile.

Results and Analysis

Synthesis of L^7BQ ligand. Given the observed ligand oxidative decay pathway of $[Mn^{III}(O_2)(MeTPEN)]^+$,[41] the L^7BQ ligand was designed in order to generate a peroxomanganese(III) adduct lacking benzylic linkers. The synthesis of this ligand involved the coupling of two quinolinyl moieties with both secondary amine groups in homopiperazine (Scheme 3). Coupling of secondary amines with aryl halides can be attained via the Pd-catalyzed Buchwald-Hartwig cross-coupling reactions.[70-72] In this case, 8-bromoquinoline and

homopiperazine could be coupled to generate the desired aminoquinolinyl L^7BQ ligand in moderate yields (~69%).

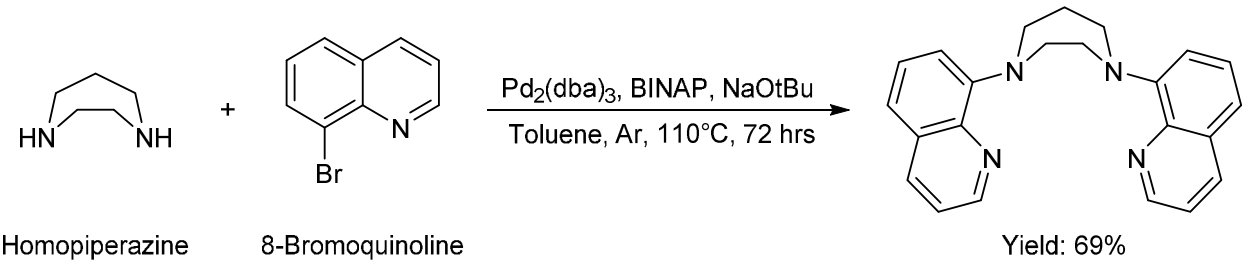

Scheme 3. Synthetic scheme for the L^7BQ ligand.

Structural Properties of $[Mn^{II}(L^7BQ)(OTf)_2]$. The $[Mn^{II}(L^7BQ)(OTf)_2]$ complex could be readily generated by the reaction of $[Mn(OTf)_2(MeCN)_2]_n$ with the L^7BQ ligand. The XRD structure of $[Mn^{II}(L^7BQ)(OTf)_2]$ contains a six-coordinate manganese center (Figure 2) in a pseudo-octahedral geometry. Significant bond lengths and angles of $[Mn^{II}(L^7BQ)(OTf)_2]$ are summarized in Table 1. In this structure, the L^7BQ ligand is coordinated in a tetradentate fashion occupying the equatorial plane (N1 - N4), with the Mn^{II} ion being displaced by 0.08 Å from the mean plane through these four coordinated nitrogens. The axial sites are occupied by the two triflate ions with an O11–Mn–O21 bond angle of 155.06°. The Mn–N distances vary between 2.2 – 2.3 Å, with the amine Mn-N distances being longer than the aromatic Mn-N distances; the Mn–O distances are ~2.2 Å (Table 1). All of these are values typical for high-spin Mn^{II} centers.[31, 34, 73] A highly distorted 6-coordinate geometry for the Mn^{II} center in $[Mn^{II}(L^7BQ)(OTf)_2]$ is indicated by the angles between coordinated atoms: N–Mn–N, 71° to 137°; O–Mn–N, 81° - 111°; and O–Mn–O, 155.06°. These angles for the MnO_2N_4 polyhedron more closely resemble a pentagonal bipyramid with a missing equatorial ligand than an octahedron. This polyhedron would ideally have equatorial N–Mn–N angles of 72° and 144°, O–Mn–N angles of 90° and an O–Mn–O angle of 180°. Nonbonded O---H interactions between

coordinated triflates and the ethyl and propyl linkers joining N2 and N3 cause the triflates to move off the vertical axis in this molecule toward the "missing" equatorial coordination site. Even though the N1---N4 separation is 4.09 Å, an acetonitrile solvent molecule of crystallization present in the asymmetric unit does not interact with the metal center (Mn–N distance of 6.729 Å) and is not shown in Figure 2. Hydrogen atoms on the two carbons adjacent to N1 and N4 are separated by 3.51 Å and block access to the fifth equatorial coordination site. The bond angles observed for $[Mn^{II}(L^7BQ)(OTf)_2]$ are very similar to those previously observed for Mn^{II} complexes of the $L^7py_2^R$ ligands.[31-32, 34]

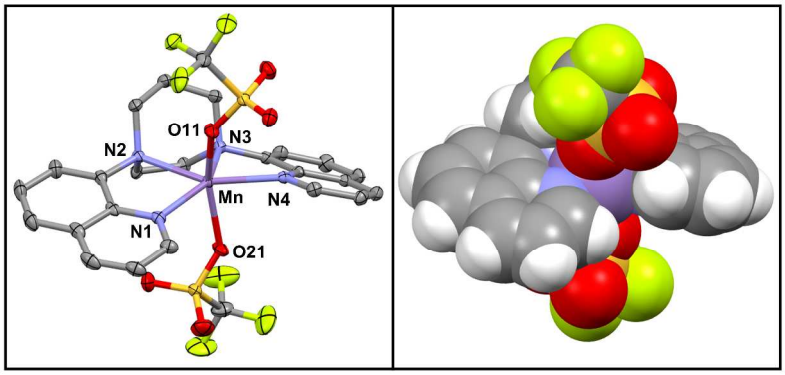

Figure 2. ORTEP diagram (left; 50% thermal probability) and space-filling model (right) for $[Mn^{II}(L^7BQ)(OTf)_2]$. Hydrogen atoms and the non-coordinating solvent molecule have been removed for clarity. Coordination bond lengths and angles are listed in Table 1.

Table 1. Selected Bond Lengths and Angles for $[Mn^{II}(L^7BQ)(OTf)_2]$.

Bond Length (Å)			
Mn–N1	2.1846(14)	Mn–N4	2.2109(14)
Mn–N2	2.3011(15)	Mn–N3	2.2841(14)
Mn–O11	2.1869(12)	Mn–O21	2.2152(13)
Bond Angle (°)			
O11–Mn–O21	155.05(5)	N4–Mn–O21	81.48(5)
N1–Mn–O11	85.22(5)	N1–Mn–N2	76.73(5)
N2–Mn–O11	95.27(5)	N2–Mn–N3	71.47(5)
N3–Mn–O11	111.49(5)	N3–Mn–N4	75.84(5)
N4–Mn–O11	88.82(5)	N1–Mn–N3	145.04(5)
N1–Mn–O21	86.37(5)	N2–Mn–N4	146.23(5)
N2–Mn–O21	105.57(5)	N1–Mn–N4	137.04(5)
N3–Mn–O21	88.43(5)		

Oxidation of $[Mn^{II}(L^7BQ)(OTf)_2]$ by H_2O_2. The electronic absorption spectrum of $[Mn^{II}(L^7BQ)(OTf)_2]$ in MeCN at 25 °C is featureless in the visible region, only showing the onset of intense absorption features at wavelengths below 400 nm (Figure 3, left). The reaction of a 2.5 mM solution of $[Mn^{II}(L^7BQ)(OTf)_2]$ with 5 equiv. H_2O_2 and 1.0 equiv. Et_3N in MeCN at -40 ^oC gives rise to a new species characterized by two prominent absorption bands centered at 450 nm (ε = 260 M^{-1} cm^{-1}) and 660 nm (ε = 75 M^{-1} cm^{-1}; Figure 3, left).[74] The intensity of the feature at 450 nm and the peak to trough ratio between 560 and 660 nm were observed to vary to a small degree between sample preparations (0.7:1 – 1:1), due to the temperature sensitive nature of the peroxo. The positions and intensities of the bands at 450 and 660 nm are strikingly similar to those of other side-on peroxomanganese(III) complexes prepared using analogous N4 ligands and similar reaction conditions.[31-32, 34] The mass spectrum of the solution of $[Mn^{II}(L^7BQ)(OTf)_2]$ following treatment with H_2O_2 and Et_3N displays an ion peak at 441.1135 *m/z* (Figure S7), which compares well with that expected for $[Mn^{III}(O_2)(L^7BQ)]^+$ (calc. = 441.1123 *m/z*). When $H_2{}^{18}O_2$ was used to generate the peroxo intermediate, the corresponding ion peak shifted to 445.1156 *m/z* (Figure S8), providing further evidence for the presence of a peroxo ligand derived from H_2O_2. It should be noted that these peaks corresponding to the Mn^{III}-peroxo intermediates are of modest intensity in the mass spectrometric data collected at room temperature. This is anticipated, given the low thermal stability of this intermediate at temperatures higher than -40 ^oC (*vide infra*).

The $[Mn^{III}(O_2)(L^7BQ)]^+$ complex was further characterized by X-band EPR spectroscopy. As integer spin systems, high-spin Mn^{III} centers (S = 2) do not show signals in perpendicular-mode EPR experiments. Parallel-mode signals have been observed for some, but certainly not all, of

the reported Mn^{III}-peroxo adducts.[37, 40-41, 75] A moderate zero-field splitting can render Mn^{III} centers silent even in parallel-mode at X-band frequencies. In contrast, mononuclear Mn^{II} and spin-coupled $Mn^{III}Mn^{III}$ and $Mn^{III}Mn^{IV}$ adducts will show prominent signals in perpendicular mode.

The perpendicular-mode EPR spectrum of $[Mn^{II}(L^7BQ)(OTf)_2]$ shows a positive feature at ca. 220 mT and a six-line signal centered near 350 mT. The six-line signal shows an average hyperfine splitting of 9.3 mT. The parallel-mode X-band EPR spectrum of $[Mn^{III}(O_2)(L^7BQ)]^+$ shows no features at 5 K, which can occur for Mn^{III} compounds with large zero-field splitting (Figure S9, top right).[76] The perpendicular mode X-band EPR spectra of $[Mn^{III}(O_2)(L^7BQ)]^+$ collected at 5 K (the red trace in Figure 3, right), reveals a low-intensity derivative-shaped signal at 350 mT and a weak feature at 220 mT (this latter feature is more apparent in a zoomed-in spectrum shown in Figure S9, bottom). These signals are most likely associated with unreacted $[Mn^{II}(L^7BQ)(OTf)_2]$, as an overlay of the perpendicular-mode EPR spectra of $[Mn^{II}(L^7BQ)(OTf)_2]$ with that of the $[Mn^{III}(O_2)(L^7BQ)]^+$ solution reveal strong similarities (Figure S9, bottom). The dominant hyperfine features of $[Mn^{II}(L^7BQ)(OTf)_2]$ are retained in the perpendicular-mode spectrum of the $[Mn^{III}(O_2)(L^7BQ)]^+$ solution (splitting of 9.7 mT). The additional fine structure (with a smaller splitting of 6.5 mT) could be due to superhyperfine interactions associated with the nitrogen ligands of L^7BQ, which are now resolved due to the lower concentration of Mn^{II}. Importantly, spin quantification shows that the perpendicular-mode EPR signal observed for the solution of $[Mn^{III}(O_2)(L^7BQ)]$ represents only 10% of the total Mn. Thus, the EPR signal arises from a minority species, clearly establishing that the bulk of Mn in the $[Mn^{III}(O_2)(L^7BQ)]^+$ solution is EPR silent.

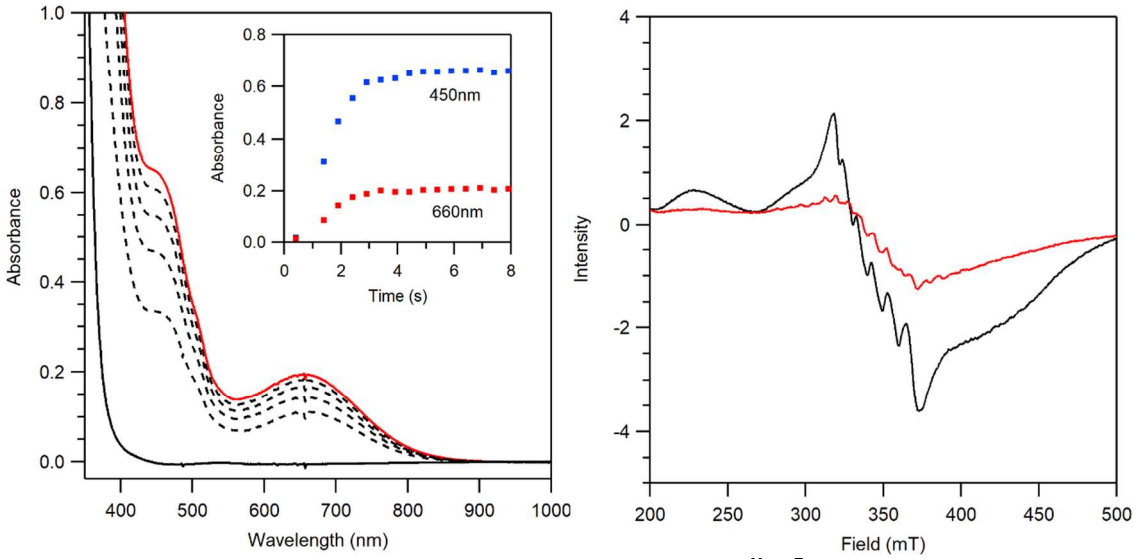

Figure 3. Left: Electronic absorption spectral changes of $[Mn^{II}(L^7BQ)(OTf)_2]$ (solid black trace) upon the addition of 5 equiv. H_2O_2 and 1.0 equiv. Et_3N in MeCN at -40 ^oC. Inset: Time evolution of absorption features at 450 nm and 660 nm. Right: Perpendicular mode X-band EPR spectra corresponding to 2.5 mM frozen MeCN solutions of $[Mn^{II}(L^7BQ)(OTf)_2]$ (solid black trace) and $[Mn^{III}(O_2)(L^7BQ)]^+$ (solid red trace) collected at 5 K.

XAS Characterization of $[Mn^{III}(O_2)(L^7BQ)]^+$. The $[Mn^{II}(L^7BQ)(OTf)_2]$ and $[Mn^{III}(O_2)(L^7BQ)]^+$ complexes showed Mn K-edge values of 6547.8 and 6549.2 eV, respectively (Table 2). The 1.6 eV lower edge energy for $[Mn^{II}(L^7BQ)(OTf)_2]$ compared to $[Mn^{III}(O_2)(L^7BQ)]^+$ is consistent with the higher Mn oxidation state for the latter complex. The edge shift is somewhat lower than that observed for other Mn^{II} and Mn^{III}-peroxo pairs (3.2 and 2.4 eV; see Table 2). However, the sample size for comparison is small, and the Mn^{II} complexes in these pairs all have different ligand spheres. Thus, variations in the Mn^{II} edges due to the different coordination environments could influence the observed shift between the Mn^{II} and Mn^{III}-peroxo species.

The pre-edge region of $[Mn^{II}(L^7BQ)(OTf)_2]$ shows one weak band at 6540.3 eV, with an area of 6.8 units. The pre-edge transitions of Mn coordination complexes arise from Mn 1s-to-3d transitions. These transitions are electric-dipole forbidden and, for low-symmetry complexes,

their intensity predominantly derives from Mn 3d-4p mixing aided by structural deviations from centrosymmetry. The small pre-edge area of $[Mn^{II}(L^7BQ)(OTf)_2]$ is consistent with a small degree of Mn 3d-4p mixing, as expected on the basis of the XRD structure (Figure 2). In contrast, the pre-edge region of $[Mn^{III}(O_2)(L^7BQ)]^+$ shows a prominent pre-edge peak at 6540.4 eV, with a shoulder at 6542.3 eV (Figure 4, inset). The total area of these peaks are 20.5 units, which is greatly increased relative to that of $[Mn^{II}(L^7BQ)(OTf)_2]$ (Table 2 and Figures 4 and S10). We had previously reported a ca. 2.5-fold increase in pre-edge area for the $[Mn^{III}(O_2)(Me_2EBC)]^+$ complex compared to its $[Mn(Cl)_2(Me_2EBC)]$ analogue (Table 2).[43] The intensity increase observed for the Mn^{II} and Mn^{III}-peroxo pair of the L^7BQ ligand is comparable, with a ca. 3-fold larger area for the latter complex.

Table 2. Edge and Pre-edge Energies (eV), Pre-edge Peak Heights and Areas for Mn^{II} and Mn^{III}-peroxo Complexes.

complex	medium	edge energy	pre-edge energy	height	area	reference
$[Mn^{II}(L^7BQ)(OTf)_2]$	MeCN	6547.8	6540.3	0.022	6.8	[a]
$[Mn^{III}(O_2)(L^7BQ)]^+$	MeCN	6549.2	6540.4, 6542.3	0.031, 0.056	20.8	[a]
$[Mn^{II}(Cl)_2(Me_2EBC)]$	solid	6547.1	6540.8	0.041	3.9	77
$[Mn^{III}(O_2)(Me_2EBC)]^+$	CH_2Cl_2	6550.3	6540.8	0.051	9.5	43
$[Mn^{II}(13\text{-TMC})]^{2+}$ [b]	CH_3CN	6545.5	NR [c]	NR [c]	NR [c]	78
$[Mn^{III}(O_2)(13\text{-TMC})]^{+}$ [b]	CH_3CN	6547.9	NR [c]	NR [c]	NR [c]	78

[a] This work. [b] 13-TMC = 1,4,7,10-tetramethyl-1,4,7,10-tetraazacyclotridecane. [c] Not reported.

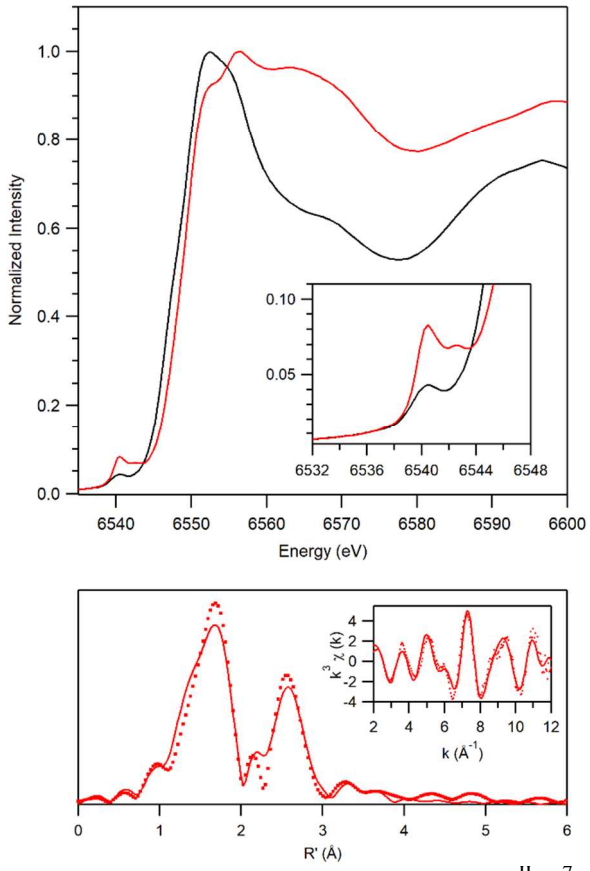

Figure 4. Top: Overlay of XANES regions for $[Mn^{II}(L^7BQ)(OTf)_2]$ (black) and $[Mn^{III}(O_2)(L^7BQ)]^+$ (red). Bottom: Fourier transform of Mn K-edge EXAFS data and raw EXAFS spectra (insets), experimental (···) and fits (—), for $[Mn^{III}(O_2)(L^7BQ)]^+$. The parameters used for the EXAFS fit are in Table 3.

The Fourier transform EXAFS spectrum of $[Mn^{III}(O_2)(L^7BQ)]^+$ consists of a prominent peak near 1.6 Å and a weaker feature at 2.7 Å (Figure 4, bottom). Results of fits to these data to obtain Mn-scatterer distances are summarized in Table 3. These features are best fit with an O shell at 1.85 Å (number of scatterers, n = 2), one N shell at 2.22 Å (n = 4) and two C shells at 3.10 and 3.59 Å (n = 5 and 3, respectively). The Mn–O distances are on the short end of those observed for crystallographically characterized Mn^{III}-peroxo adducts (Mn–O distances of 1.841 – 1.901 Å), while the Mn–N distances are typical for high-spin Mn^{III} complexes with amine, pyridine, and quinoline ligands.[12]

Table 3. EXAFS fitting results for $[Mn^{III}(O_2)(L^7BQ)]^+$ in MeCN ($\Delta k = 10$ Å^{-1}).

	Mn-O/N			Mn-N			Mn-C				
fit	n	r(Å)	σ^2	n	r(Å)	σ^2	n	r(Å)	σ^2	E_0	R
1	0			6	2.07	0.00404				-47.79	0.41
2	2	1.85	0.00413	4	2.22	0.00722				3.58	0.28
3	2	1.85	0.00367	4	2.23	0.00819	4	3.10	0.08631	4.87	0.13
4	2	1.85	0.00376	4	2.22	0.00792	4	3.59	0.00705	4.13	0.12
							6	3.10	0.00394		
5	2	1.85	0.00373	4	2.22	0.00802	3	3.59	0.00457	4.35	0.12
							6	3.10	0.00388		
6	**2**	**1.85**	**0.00373**	**4**	**2.22**	**0.00799**	**3**	**3.59**	**0.00420**	**4.13**	**0.11**
							5	**3.10**	**0.00256**		

DFT Structure of $[Mn^{III}(O_2)(L^7BQ)]^+$ and Pre-edge Properties from Time-Dependent (TD) DFT Computations. The structure of the L^7BQ ligand provides two unique faces for the peroxo unit to bind to the manganese center, one on the side of the ethyl linker and the other on the side of the propyl linker. Structures for these isomeric forms of $[Mn^{III}(O_2)(L^7BQ)]^+$ were optimized (Figure S11), and the structure with the peroxide bound on the propyl face is calculated to be 5 kcal mol^{-1} lower in energy than the structure with the peroxide bound on the ethyl face. This result is in agreement with similar computations for $[Mn^{III}(O_2)(L^7py_2^H)]^+$.[31] All values discussed here are from the lower energy structure of $[Mn^{III}(O_2)(L^7BQ)]^+$, but simulated XANES for both complexes are given in the Supporting Information (Figure S12). TD-DFT simulated UV-vis absorption spectra of $[Mn^{III}(O_2)(L^7BQ)]^+$ with the peroxide bound on the propyl face is also included in the Supporting Information (Figure S13).

Metric parameters for the DFT structure of $[Mn^{III}(O_2)(L^7BQ)]^+$ species with the peroxide bound on the propyl face are reported in the Supporting Information (Table S2). The Mn–O bond lengths are 1.862 Å and 1.856 Å, while the O–O bond is 1.418 Å. The calculated Mn–O distances are in excellent agreement with the best fit of the experimental EXAFS data, which included a 2 atom O shell at 1.85 Å (Table 3). The calculated Mn–O and O–O distances also

agree well with corresponding bond lengths for crystallographically characterized Mn^{III}-peroxo complexes, in which the Mn–O and O–O bond lengths range from 1.838 to 1.901 Å and 1.402 to 1.43 Å respectively.[12, 22-27] Additionally, the average Mn–N bond lengths of 2.22 Å for the DFT model of $[Mn^{III}(O_2)(L^7BQ)]^+$ is the same as the Mn–N distances from EXAFS (2.22 Å; see Table 3) and is accordant with corresponding bond lengths of other high-spin Mn^{III} complexes with nitrogen-based ligands. The two C shells from EXAFS analysis at 3.10 and 3.59 Å (n = 5 and 3, respectively) are also in good agreement with average distances of the closest carbons from the L^7BQ ligand determined in the DFT optimized structure, which come from the propyl and ethyl arms of the diazocycloalkane backbone as well as from several carbon atoms from the quinoline moieties (DFT distances of 2.98 – 3.54 Å).

The TD-DFT calculated pre-edge spectra for $[Mn^{III}(O_2)(L^7BQ)]^+$ shows two overlapping bands with energies of 6540.2 and 6541 eV, which is similar to the two peaks seen in the experimental pre-edge spectrum at 6540.8 and 6542.3 eV. Using a coordinate system where the Mn^{III}-O_2 unit lies in the xy plane, the first peak arises from excitations into the Mn^{III} β-$3d_{yz}$, $3d_{x2-y2}$, and $3d_{xz}$ orbitals, and the second peak arises from excitations into the Mn^{III} α-$3d_{xy}$ orbital and the Mn^{III} β-$3d_{z2}$ and $3d_{xy}$ orbitals (where α and β refer to majority and minority spin electrons, respectively). The calculated pre-edge area of 14.7 units underestimates the experimentally determined pre-edge area of 20.8 units, but reproduces an increase in area when compared to that previously calculated for the $[Mn^{III}(O_2)(Me_2EBC)]^+$ complex (Table 4). The summed Mn 4p character in the Mn 3d-based orbitals involved in the six pre-edge transitions of $[Mn^{III}(O_2)(L^7BQ)]^+$ is 3.6%, with significant contributions from multiple Mn^{III}-based orbitals. This 4p-3d mixing across the Mn^{III} 3d-manifold implies that geometric distortions induced by both the peroxo and L^7BQ ligands drive the large pre-edge area of $[Mn^{III}(O_2)(L^7BQ)]^+$. This

mechanism for orbital mixing is different than $[Mn^{III}(O_2)(Me_2EBC)]^+$, where a sizeable 4p contribution was observed only in the Mn–O peroxo σ-antibonding MO.[43]

Table 4. Experimental and TD-DFT-calculated Pre-edge Area and Mn 4p Contributions for $[Mn^{III}(O_2)(L^7BQ)]^+$ and $[Mn^{III}(O_2)(Me_2EBC)]^+$.

	experimental			calculated			ref
complex	pre-edge energy	height	area	pre-edge energy	area	Mn 4p (%)	
$[Mn^{III}(O_2)(L^7BQ)]^+$	6540.4	0.03	21	6540.2	14.7	3.6	[a]
	6542.3	0.06		6541			
$[Mn^{III}(O_2)(Me_2EBC)]^+$	6540.8	0.05	9.5	6541	6.1	3.0 [b]	43

[a]This work. [b]The percent Mn 4p-character differs from the previously published values; after re-evaluation of the computational output, it was determined that the previous value was in error.

Stability and Thermal Decay of $[Mn^{III}(O_2)(L^7BQ)]^+$. A 2.5 mM solution of $[Mn^{III}(O_2)(L^7BQ)]^+$ prepared using 5 equiv. H_2O_2 and 1.0 equiv. Et_3N in MeCN at -40 ^oC decays slowly over the course of an hour, with a half-life of ca. 10 minutes. In comparison, the $[Mn^{III}(O_2((L^7py_2)]^+$ complex is shown to be stable for several hours at -40 °C ($t_{1/2}$ = 15 minutes at 0 °C), and the identity of the decay product was not determined.[31] The decay of $[Mn^{III}(O_2)(L^7BQ)]^+$ is characterized by an increase in absorbance at 450 and 550 nm, as shown in Figure 5. The perpendicular-mode X-band EPR spectrum of this decay species is quite similar to that of $[Mn^{III}(O_2)(L^7BQ)]^+$, showing only a low-intensity derivative-shaped signal at 350 mT, with a multi-line hyperfine pattern indicative of a multinuclear manganese species along with no features in parallel mode (see Figure S14). These data suggest that the decay product is EPR silent. Thus, the decay product could be a separate monomeric Mn^{III} species or an S = 0 antiferromagnetically coupled dimer. The rate of decay of $[Mn^{III}(O_2)(L^7BQ)]^+$ is sensitive to the amount of base used to prepare the Mn^{III}-peroxo adduct, as $[Mn^{III}(O_2)(L^7BQ)]^+$ formed using triethylamine in excess of 1.0 equiv. is observed to decay more rapidly.

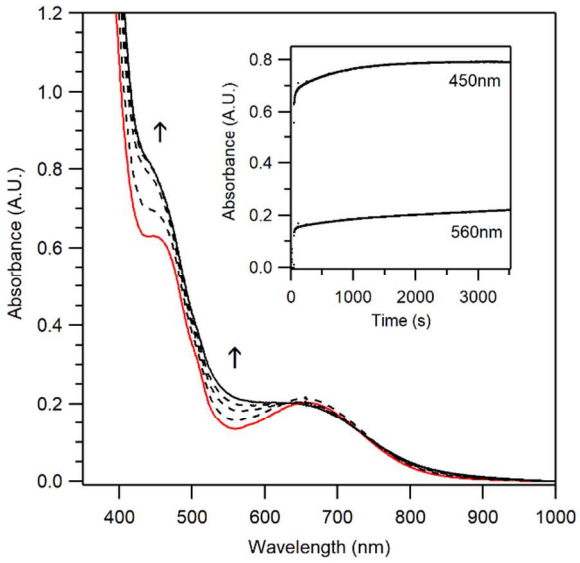

Figure 5. Electronic absorption spectral changes upon the self-decay of $[Mn^{III}(O_2)(L^7BQ)]^+$ (solid red trace) at -40°C in MeCN. Inset: Time evolution of absorption features at 450 nm and 560 nm, which highlights the formation of a decay species over 50 minutes.

We have previously reported that the decay pathways of the Mn^{III}-peroxo adducts $[Mn^{III}(O_2)(\kappa^4\text{-N4py})]^+$ and $[Mn^{III}(O_2)(Me_2EBC)]^+$ proceed by reaction of the Mn^{III}-peroxo center with unreacted Mn^{II} starting material.[35, 43] To investigate if this decay pathway is possible for the $[Mn^{III}(O_2)(L^7BQ)]^+$ complex, we added 1.0 equiv. of $[Mn^{II}(L^7BQ)(OTf)_2]$ to $[Mn^{III}(O_2)(L^7BQ)]^+$ at -40°C, after the latter had maximally formed. We observed no change in the electronic absorption spectrum upon the addition of the Mn^{II} complex, and the $[Mn^{III}(O_2)(L^7BQ)]^+$ species continued along its self-decay path (see Figure S15). Thus, the decay of $[Mn^{III}(O_2)(L^7BQ)]^+$ does not occur by reaction with the Mn^{II} starting material.

We also explored the formation of $[Mn^{III}(O_2)(L^7BQ)]^+$ over a variety of temperatures (-40 °C to room temperature) in different solvents (including methanol, propionitrile, butyronitrile, ethanol, dichloromethane, tetrahydrofuran and 2-methyltetrahydrofuran). Of these solvents, $[Mn^{III}(O_2)(L^7BQ)]^+$ could only be generated in propionitrile, but the species was much less stable. When formed in propionitrile at -40 °C, the electronic absorption bands associated with

the Mn^{III}-peroxo species at 450 and 660 nm loses definition within 15 seconds, indicating a substantially more rapid decay in this solvent (the half-life here is estimated to be ca. 1 minute). The limited variability of the solvent and temperature for $[Mn^{III}(O_2)(L^7BQ)]^+$ formation has prevented additional spectroscopic characterization. For example, characterization of $[Mn^{III}(O_2)(L^7BQ)]^+$ by magnetic circular dichroism (MCD) spectroscopy is not feasible due to the poor glassing capabilities of MeCN. We have previously shown that MCD spectroscopy can provide useful insights into understanding the geometric and electronic structures of peroxomanganese(III) species.[28, 31, 34] Furthermore, unlike the closely related $[Mn^{III}(O_2)(L^7py_2^R)]^+$ series of peroxo compounds,[31, 34] $[Mn^{III}(O_2)(L^7BQ)]^+$ could not be generated using KO_2 as the oxidant.

Reactivity of $[Mn^{III}(O_2)(L^7BQ)]^+$ with aldehydes. When a 2.5 mM solution of $[Mn^{III}(O_2)(L^7BQ)]^+$ at -40 °C in MeCN is treated with an excess (165 equivalents) of cylcohexanecarboxaldehyde (CCA), the absorption features for the peroxomanganese(III) species decay (Figure 6, left). Analysis of the resulting solution by GC-MS showed cyclohexanone in 38% yield compared to the starting concentration of $[Mn^{II}(L^7BQ)(OTf)_2]$. The formation and percent yield of cyclohexanone are similar to those previously reported for CCA deformylation by other Mn^{III}-peroxo complexes.[32, 37] We attempted to investigate the kinetics of the reaction of $[Mn^{III}(O_2)(L^7BQ)]^+$ with CCA by following the disappearance of the Mn^{III}-peroxo electronic absorption bands at 450 and 660 nm (Figure 6, left). This approach was used previously to determine second-order rate constants for the reactions of $[Mn^{III}(O_2)(L^7py_2^R]^+$ complexes with CCA.[31] However, the disappearance of the electronic absorption bands associated with $[Mn^{III}(O_2)(L^7BQ)]^+$ upon the addition of excess CCA did not follow pseudo-first-order behavior. Instead, we observed a rapid initial drop in absorption intensity within the first 5

seconds of the reaction, followed by a slow decay (Figure 6, left inset). Furthermore, this rapid drop led to the appearance of a new chromophore, which we have termed intermediate A, with band maxima at 595 and 450 nm (Figure 6, left, blue trace). This kinetic behavior suggests that $[Mn^{III}(O_2)(L^7BQ)]^+$ shows an initial rapid reaction with CCA to give a new intermediate that then more slowly decays.

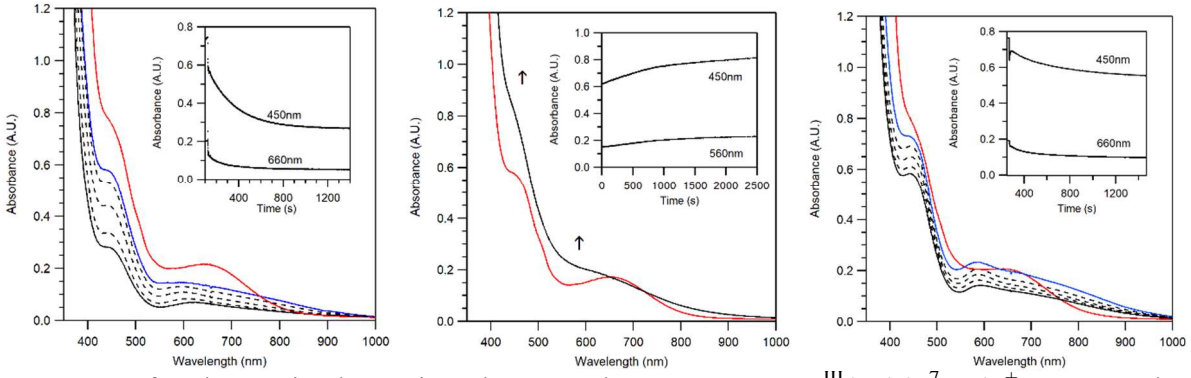

Figure 6. Left: Electronic absorption changes when 2.5 mM $[Mn^{III}(O_2)(L^7BQ)]^+$ are treated with 165 equiv. CCA in MeCN at -40°C. Center: Electronic absorption changes when 2.5 mM $[Mn^{III}(O_2)(L^7BQ)]^+$ are treated with 40 equiv. pure PPA in MeCN at -40°C. Right: Electronic absorption changes when 2.5 mM $[Mn^{III}(O_2)(L^7BQ)]^+$ are treated with 40 equiv. acid-contaminated PPA in MeCN at -40°C.

To better understand this deformylation chemistry, we also explored the reactivity of $[Mn^{III}(O_2)(L^7BQ)]^+$ with the aldehyde PPA. Unexpectedly, the addition of 40 equivalents of PPA to a 2.5 mM solution of $[Mn^{III}(O_2)(L^7BQ)]^+$ at -40 °C in MeCN did not show evidence of a reaction but instead followed the self-decay pathway of $[Mn^{III}(O_2)(L^7BQ)]^+$ (Figure 6, center). Additional analysis provided no evidence for the formation of the expected deformylation product (acetophenone) under these conditions. Further investigations showed that this lack of reactivity was highly dependent on the purity of PPA. Only in cases where PPA lacked any acid impurities did $[Mn^{III}(O_2)(L^7BQ)]^+$ fail to show a reaction with PPA. In cases where acid impurities where present (as assessed by ^{1}H-NMR investigations of PPA; see Figure S16), the addition of PPA to $[Mn^{III}(O_2)(L^7BQ)]^+$ resulted in electronic absorption changes very similar to

those observed when $[Mn^{III}(O_2)(L^7BQ)]^+$ was treated with CCA. Specifically, the signals associated with $[Mn^{III}(O_2)(L^7BQ)]^+$ show a rapid initial change to give an intermediate with features near 595 and 450 nm (blue trace), and this new chromophore would slowly decay (Figure 6, right). In addition, acetophenone formation was observed only for reactions of $[Mn^{III}(O_2)(L^7BQ)]^+$ with PPA containing acid contaminants.

On the basis of these observations, we attribute the initial rapid change in the electronic absorption spectrum of $[Mn^{III}(O_2)(L^7BQ)]^+$ when treated with CCA (or PPA with acid impurity) to a reaction of the Mn^{III}-peroxo unit with acid. McDonald and co-workers have noted that CCA commonly contains a small percentage of cyclohexanecarboxylic acid, which is challenging to completely remove by distillation.[79] ^{1}H-NMR experiments performed for CCA before and after distillation show the persistent of both formic acid and cyclohexanecarboxylic acid (Figure S17).

To test our hypothesis that an acid impurity accounts for the initial reaction of $[Mn^{III}(O_2)(L^7BQ)]^+$ with CCA, we investigated the reactivity of $[Mn^{III}(O_2)(L^7BQ)]^+$ with cyclohexanecarboxylic acid. For this reaction, we used concentrations of cyclohexanecarboxylic acid (2 equivalents relative to Mn) comparable to those present when 165 equivalents CCA are added to $[Mn^{III}(O_2)(L^7BQ)]^+$. From these experiments, we found that when a 2.5 mM solution of $[Mn^{III}(O_2)(L^7BQ)]^+$ is treated with 2.0 equivalents of cyclohexanecarboxylic acid in MeCN at -40 °C, the electronic absorption signals associated with $[Mn^{III}(O_2)(L^7BQ)]^+$ were replaced with new features at 580 and 450 nm (Figure 7, left). This process is complete within 10 seconds. The electronic absorption features of this new intermediate are almost identical to those of intermediate A (see Figure 7, right). Under these conditions, the intermediate formed from the reaction of $[Mn^{III}(O_2)(L^7BQ)]^+$ with cyclohexanecarboxylic acid is stable for over 100 seconds at -40 °C in MeCN, which permitted its further characterization by additional spectroscopic

methods. On the basis of the disappearance of the optical features of intermediate A, the half-life of this species is ca. 10 minutes.

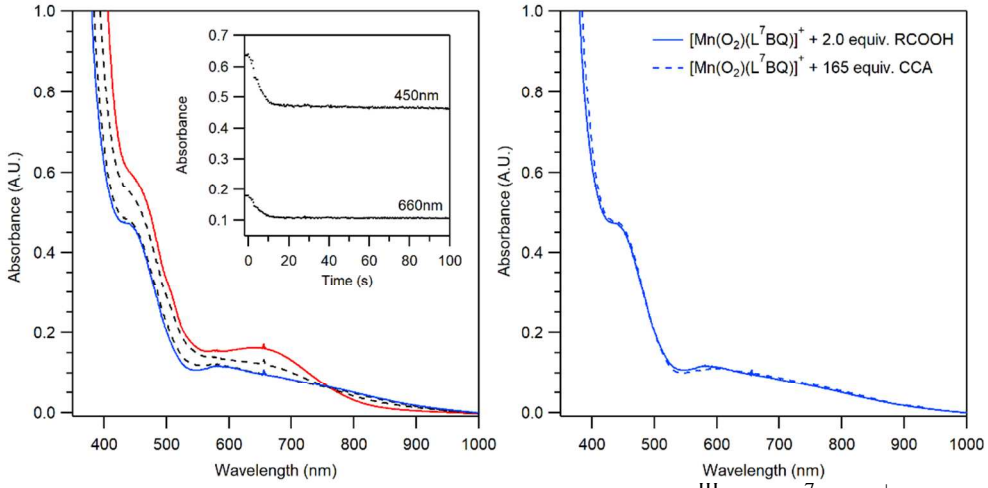

Figure 7. Left: Electronic absorption changes for $[Mn^{III}(O_2)(L^7BQ)]^+$ + 2 equiv. cyclohexanecarboxylic acid in MeCN at -40 °C to generate a new species (solid blue trace). Right: Overlay of electronic absorption features of the new species (solid blue trace) and intermediate A formed from the treatment of $[Mn^{III}(O_2)(L^7BQ)]^+$ with excess CCA (dashed blue trace).

Combined EPR and XAS characterization of intermediate A reveal spectroscopic signatures associated with $[Mn^{II}(L^7BQ)(OTf)_2]$ in MeCN. For example, no signals were observed for intermediate A in the parallel-mode spectrum at X-band frequency, but perpendicular-mode data revealed the presence of a six-line feature, centered at 350 mT, that is essentially identical in appearance to that of $[Mn^{II}(L^7BQ)(OTf)_2]$ in MeCN (Figure S18). Spin quantification of the 6-line signal of intermediate A relative to $[Mn^{II}(L^7BQ)(OTf)_2]$ in MeCN indicates that the signal represents 80 ± 15% of the Mn in the sample. However, as $[Mn^{II}(L^7BQ)(OTf)_2]$ is colorless, a minority species, which is not observed by EPR spectroscopy, must give rise to the electronic absorption signals of intermediate A at 450 and 595 nm. XAS data collected for intermediate A reveal XANES data significantly perturbed relative to $[Mn^{III}(O_2)(L^7BQ)]^+$, but very similar to those of $[Mn^{II}(L^7BQ)(OTf)_2]$ in MeCN (Figure S19). Notably, the XANES data of intermediate

A are not identical to those of $[Mn^{II}(L^7BQ)(OTf)_2]$, suggesting the presence of additional Mn species. Collectively, the EPR and XAS data suggest that the species responsible for the 450 and 595 nm electronic absorption bands of intermediate A represents a small fraction of the total Mn in the sample, with the bulk of Mn having reverted back to the Mn^{II} starting material.

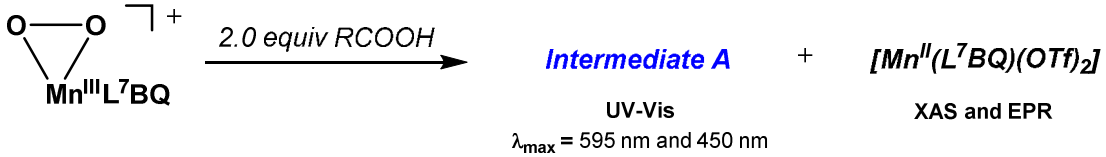

Scheme 4. Summary of reactivity observed upon addition of cyclohexanecaboxylic acid to $[Mn^{III}(O_2)(L^7BQ)]^+$.

As we can observe intermediate A by electronic absorption spectroscopy, we are able to monitor the response of this species to added aldehydes. When $[Mn^{III}(O_2)(L^7BQ)]^+$ with 2 equiv. cyclohexanecarboxylic acid are treated with 40 equivalents of PPA, we observe the formation of a small amount of acetophenone (10% relative to the starting Mn concentration). These observations suggest that intermediate A is competent for aldehyde deformylation.

Discussion.

Peroxomanganese(III) adducts have been proposed as key intermediates for a number of manganese-dependent enzymes, as well as for small-molecule catalysts featuring manganese centers.[1-6, 15-16, 80] Compared to analogous iron systems, mechanistic knowledge of manganese-dependent biological processes is still rather limited. Furthermore, due to numerous challenges involved in enzymatic studies, small-molecule model complexes of Mn enzymes have been widely used to understand the properties of these enzymes.[12, 34-35, 81-84] Although η^2-peroxomanganese(III) complexes are the most common example of Mn-peroxo species,[22-28, 31-41]

η^1-alkylperoxomanganese(III), η^1-hydroperoxomanganese(III), and *trans*-μ-1,2-peroxo-bridged dimanganese(III,III) dimeric species have also been structurally and/ or spectroscopically characterized.[29-30, 85] However, a limitation in the thorough characterization of the structural properties and chemical reactivity of these complexes stem from their commonly observed low chemical yields and impaired thermal stability.[12]

Sastri and co-workers have recently shown that a Mn^{III}-peroxo adduct supported by a neutral N_5 ligand is able to deformylate PPA by a hydrogen-atom transfer mechanism involving attack at the weak benzylic C–H bond of the substrate.[45] This work suggested that a Mn^{III}-peroxo adduct supported by a ligand with benzylic C–H bonds may be especially susceptible to ligand degradation. Motivated by these observations, we designed the L^7BQ ligand, which features a topology similar to that of the $L^7py_2^R$ family that has shown much success in supporting Mn^{III}-peroxo ligands, but lacks the benzylic arms, which may be prone to oxidation.[31-32, 34]

The Mn^{II} complex of the new L^7BQ ligand, $[Mn^{II}(L^7BQ)(OTf)_2]$, was structurally characterized by X-ray diffraction. As anticipated, the structure of this complex is similar to the related Mn^{II} salts of the $L^7py_2^R$ ligand family.[31-32, 34] When treated with 5 equiv. of H_2O_2 and 1.0 equiv. of triethylamine, $[Mn^{II}(L^7BQ)(OTf)_2]$ produced a new intermediate in MeCN solution at -40 ^oC. Electronic absorption and EPR spectroscopy, mass spectrometry, and Mn K-edge XAS data provide support for the formulation of this intermediate as the mononuclear Mn^{III}-peroxo adduct $[Mn^{III}(O_2)(L^7BQ)]^+$. This intermediate must be generated at cryogenic temperatures and decays over the course of 50 minutes at -40 °C in MeCN. Unlike several other Mn^{III}-peroxo adducts, the decay of $[Mn^{III}(O_2)(L^7BQ)]^+$ does not appear to be through the reaction with the Mn^{II} starting material.

The half-life of $[Mn^{III}(O_2)(L^7BQ)]^+$ at -40 °C in MeCN is ca. 10 minutes. Thus, $[Mn^{III}(O_2)(L^7BQ)]^+$ does not display enhanced thermal stability relative to its $[Mn^{III}(O_2)(L^7py_2^R)]^+$ analogues (the $[Mn^{III}(O_2)(L^7py_2^H)]^+$ complex was stable for hours at -40 °C and had a half-life of 15 minutes at 0 °C).[31] For both $[Mn^{III}(O_2)(L^7BQ)]^+$ and $[Mn^{III}(O_2)(L^7py_2^R)]^+$ complexes, the products of thermal decay have not been identified.[31] In addition to the different thermal stabilities, the $[Mn^{III}(O_2)(L^7BQ)]^+$ complex also showed reactivity with aldehydes distinct from that of the $[Mn^{III}(O_2)(L^7py_2^R)]^+$ complexes. Treatment of the $[Mn^{III}(O_2)(L^7py_2^R)]^+$ complexes with aldehydes (such as CCA and benzaldehydes) led to a decay that followed pseudo-first-order behavior. Experiments using different concentrations of CCA showed an increased decay rate with increasing CCA concentration, which permitted the determination of second-order rate constants.[32]

Unlike those systems, the reaction of $[Mn^{III}(O_2)(L^7BQ)]^+$ and CCA did not follow pseudo-first-order kinetics. Instead, the addition of CCA led to the rapid formation of intermediate A, characterized by band maxima at 595 and 450 nm (Figure 6, left). This intermediate then slowly decayed. Nonetheless, analysis of the solution obtained at the end of the reaction provided evidence for roughly 40% cyclohexanone formation, suggestive of aldehyde deformylation. Additional experiments showed that the intermediate observed by electronic absorption spectroscopy (intermediate A) resulted from the reaction of $[Mn^{III}(O_2)(L^7BQ)]^+$ with acid impurity present in CCA.

McDonald and coworkers have previously emphasized the challenge in assigning the identity of the active metal species in reactions with aldehydes precisely because of the persistence of acid impurities in aldehyde substrates.[79] Our present observations underscore this point. Here, we provide strong evidence that acid impurities in CCA convert the $[Mn^{III}(O_2)(L^7BQ)]^+$ species to a

new, colored intermediate. Additional spectroscopic data also suggest the reaction of $[Mn^{III}(O_2)(L^7BQ)]^+$ with acid regenerates the corresponding Mn^{II} complex, with the chromophoric intermediate representing only ~20% of Mn in the sample (Scheme 4).

While the identity of this intermediate is unclear, we postulate that this new intermediate, and not $[Mn^{III}(O_2)(L^7BQ)]^+$, is responsible for the observed deformylation reactivity. Support for this proposal is provided by the reactions of $[Mn^{III}(O_2)(L^7BQ)]^+$ with PPA. When $[Mn^{III}(O_2)(L^7BQ)]^+$ is treated with purified PPA, lacking acid impurities, we observe no reaction. In contrast, when $[Mn^{III}(O_2)(L^7BQ)]^+$ is treated with PPA that contains acid impurities, we observe changes in the electronic absorption spectrum consistent with the formation of intermediate A, and this intermediate decays further. Moreover, $[Mn^{III}(O_2)(L^7BQ)]^+$ treated first with 2 equiv. cyclohexanecarboxylic acid and then PPA shows evidence for a small amount of acetophenone, the expected product of PPA deformylation.

One of several possibilities for the identity of intermediate A is a Mn^{III}-hydroxperoxo adduct. To the best of our knowledge, the only examples of well-characterized Mn^{III}-hydroxoperoxo adducts come from the work of Nam and coworkers.[78, 86] By protonating the corresponding Mn^{III}-peroxo species, they have generated the $[Mn^{III}(OOH)(14\text{-TMC})]^+$ and $[Mn^{III}(OOH)(13\text{-TMC})]^+$ complexes (where 13-TMC is 1,,4,7,10-tetramethyl-1,4,7,10-tetraazacyclotridecane and 14-TMC is 1,4,8,11-tetramethyl-1,4,8,11-tetraazacyclotetradecane).[78, 86] Kinetic investigations have revealed that the Mn^{III}-hydroperoxo adducts react more rapidly with CCA than their Mn^{III}-peroxo counterparts. Specifically, the second-order rate constants (k_2) for the reactions of $[Mn^{III}(OOH)(13\text{-TMC})]^+$ and $[Mn^{III}(O_2)(13\text{-TMC})]^+$ with CCA are, respectively, $1.2(1) \times 10^{-1}$ M^{-1} s^{-1} (at -10 °C) and $2.0(1) \times 10^{-2}$ M^{-1} s^{-1} (at 10 °C). In addition, the reaction of acid with $[Mn^{III}(O_2)(14\text{-TMC})]^+$ to generate $[Mn^{III}(OOH)(14\text{-TMC})]^+$ was quite rapid compared to both of

these processes. Thus, in cases where acid impurities are present in the aldehyde substrate, it could be that the metal-hydroperoxo adduct, rather than the metal-peroxo, is the active species for aldehyde deformylation.

Similar kinetic studies have been performed for iron systems, where there are also examples of interconversion of Fe^{III}-peroxo and Fe^{III}-hydroperoxo adducts using acid-base chemistry.[87-88] Most relevant to this present work are investigations of the reactivity of Fe^{III}-peroxo and Fe^{III}-hydroperoxo adducts of the 14-TMC ligand with aldehydes. Specifically, the $[Fe^{III}(OOH)(14\text{-}TMC)]^{+}$ complex was observed to readily react with PPA at low temperatures, whereas the corresponding $[Fe^{III}(O_2)(14\text{-}TMC)]^{+}$ complex only reacted with PPA at higher temperatures. The higher nucleophilic reactivity of the iron-hydroperoxo species was attributed to the end-on binding mode. The same trend was observed for electrophilic reactions, where the Fe^{III}-hydroperoxo was more active towards weak C–H bonds than the Fe^{III}-peroxo species.[88]

Thus, it has been seen in both Fe and Mn chemistry that metal(III)-peroxo and metal(III)-hydroperoxo adducts can have large, and somewhat unexpected, differences in reaction rates with aldehydes substrates. Given these collective observations, we echo McDonald in suggesting that the role of acid impurities in obfuscating understanding of aldehyde reactivity should be considered in all studies of aldehyde deformylation by metal-peroxo complexes.[79]

Acknowledgements: This work was supported by the U.S. NSF (CHE-1565661). M.C.D. was supported by the NIH Graduate Traineeship T32 GM08545. The U.S. NSF is acknowledged for funds used for the purchase of the EPR spectrometer (CHE-0946883). Support for the NMR instrumentation was provided by NIH Shared Instrumentation Grant # S10OD016360 and NIH Shared Instrumentation Grant #S10RR014767. Use of the Stanford Synchrotron Radiation

Lightsource, SLAC National Accelerator Laboratory, is supported by the U.S. Department of Energy, Office of Science, Office of Basic Energy Sciences under Contract No. DE-AC02-76SF00515. The SSRL Structural Molecular Biology Program is supported by the DOE Office of Biological and Environmental Research, and by the National Institutes of Health, National Institute of General Medical Sciences (including P41GM103393). The contents of this publication are solely the responsibility of the authors and do not necessarily represent the official views of NIGMS or NIH. XAS experiments at Brookhaven National Lab were supported by the Case Western Reserve University Center for Synchrotron Biosciences NIH grant, P30-EB-009998, from the National Institute of Biomedical Imaging and Bioengineering (NIBIB). The NSF (CHE-0923449) and the University of Kansas are acknowledged funds to purchase the X-ray instrumentation, computers, and software used in this study.

References

1. Miller, A.-F., Superoxide Dismutases: Active Sites that Save, but a Protein that Kills. *Curr. Opin. Chem. Biol.* **2004,** *8*, 162-168.
2. Grove, L. E.; Brunold, T. C., SECOND-SPHERE TUNING OF THE METAL ION REDUCTION POTENTIALS IN IRON AND MANGANESE SUPEROXIDE DISMUTASES. *Comments on Inorganic Chemistry* **2008,** *29* (5/6), 134-168.
3. Koehntop, K. D.; Emerson, J. P.; Que, L., Jr., The 2-His-1carboxylate facial triad: a versatile platform for dioxygen activation by mononuclear non-heme iron(II) enzymes. *J. Biol. Inorg. Chem.* **2005,** *10* (2), 87-93.
4. Gunderson, W. A.; Zatsman, A. I.; Emerson, J. P.; Farquhar, E. R.; Que, L.; Lipscomb, J. D.; Hendrich, M. P., Electron Paramagnetic Resonance Detection of Intermediates in the Enzymatic Cycle of an Extradiol Dioxygenase. *J. Am. Chem. Soc.* **2008,** *130* (44), 14465-14467.
5. Borowski, T.; Bassan, A.; Richards, N. G. J.; Siegbahn, P. E. M., Catalytic Reaction Mechanism of Oxalate Oxidase (Germin). A Hybrid DFT Study. *Journal of Chemical Theory and Computation* **2005,** *1* (4), 686-693.
6. Opaleye, O.; Rose, R.-S.; Whittaker, M. M.; Woo, E.-J.; Whittaker, J. W.; Pickersgill, R. W., Structural and Spectroscopic Studies Shed Light on the Mechanism of Oxalate Oxidase. *Journal of Biological Chemistry* **2006,** *281* (10), 6428-6433.
7. Tabares, L. C.; Gätjens, J.; Hureau, C.; Burrell, M. R.; Bowater, L.; Pecoraro, V. L.; Bornemann, S.; Un, S., pH-Dependent Structures of the Manganese Binding Sites in Oxalate Decarboxylase as Revealed by High-Field Electron Paramagnetic Resonance. *J. Phys. Chem. B* **2009,** *113* (26), 9016-9025.

8. Tanner, A.; Bowater, L.; Fairhurst, S. A.; Bornemann, S., Oxalate Decarboxylase Requires Manganese and Dioxygen for Activity: OVEREXPRESSION AND CHARACTERIZATION OF BACILLUS SUBTILIS YvrK AND YoaN. *J. Biol. Chem.* **2001,** *276* (47), 43627-43634.
9. Wu, A. J.; Penner-Hahn, J. E.; Pecoraro, V. L., Structural, Spectroscopic, and Reactivity Models for the Manganese Catalases. *Chem. Rev.* **2004,** *104* (2), 903-938.
10. Cotruvo, J. A.; Stich, T. A.; Britt, R. D.; Stubbe, J., Mechanism of Assembly of the Dimanganese-Tyrosyl Radical Cofactor of Class Ib Ribonucleotide Reductase: Enzymatic Generation of Superoxide Is Required for Tyrosine Oxidation via a Mn(III)Mn(IV) Intermediate. *J. Am. Chem. Soc.* **2013**.
11. Cotruvo, J. J. A.; Stubbe, J., Metallation and mismetallation of iron and manganese proteins in vitro and in vivo: the class I ribonucleotide reductases as a case study. *Metallomics* **2012,** *4* (10), 1020-1036.
12. Leto, D.; Jackson, T., Peroxomanganese complexes as an aid to understanding redox-active manganese enzymes. *Journal of Biological Inorganic Chemistry* **2014,** *19* (1), 1-15.
13. Baglia, R. A.; Zaragoza, J. P. T.; Goldberg, D. P., Biomimetic Reactivity of Oxygen-Derived Manganese and Iron Porphyrinoid Complexes. *Chemical Reviews* **2017,** *117* (21), 13320-13352.
14. Jasniewski, A. J.; Que, L., Dioxygen Activation by Nonheme Diiron Enzymes: Diverse Dioxygen Adducts, High-Valent Intermediates, and Related Model Complexes. *Chemical Reviews* **2018,** *118* (5), 2554-2592.
15. Sibbons, K. F.; Shastri, K.; Watkinson, M., The application of manganese complexes of ligands derived from 1,4,7-triazacyclononane in oxidative catalysis. *Dalton Trans.* **2006,** (5), 645-661.
16. Saisaha, P.; de Boer, J. W.; Browne, W. R., Mechanisms in manganese catalysed oxidation of alkenes with H2O2. *Chem. Soc. Rev.* **2013,** *42* (5), 2059-2074.
17. Ottenbacher, R. V.; Samsonenko, D. G.; Talsi, E. P.; Bryliakov, K. P., Enantioselective Epoxidations of Olefins with Various Oxidants on Bioinspired Mn Complexes: Evidence for Different Mechanisms and Chiral Additive Amplification. *ACS Catalysis* **2016,** *6* (2), 979-988.
18. Ottenbacher, R.; Talsi, E.; Bryliakov, K., Direct Selective Oxidative Functionalization of C–H Bonds with H2O2: Mn-Aminopyridine Complexes Challenge the Dominance of Non-Heme Fe Catalysts. *Molecules* **2016,** *21* (11), 1454.
19. Talsi, E. P.; Ottenbacher, R. V.; Bryliakov, K. P., Bioinspired oxidations of aliphatic C–H groups with H2O2 in the presence of manganese complexes. *Journal of Organometallic Chemistry* **2015,** *793*, 102-107.
20. Codola, Z.; Lloret-Fillol, J.; Costas, M., Aminopyridine iron and manganese complexes as molecular catalysts for challenging oxidative transformations. *Prog. Inorg. Chem.* **2014,** *59* (Copyright (C) 2016 American Chemical Society (ACS). All Rights Reserved.), 447-531.
21. Company, A.; Lloret-Fillol, J.; Costas, M. In *Small molecule models for nonporphyrinic iron and manganese oxygenases*, Elsevier B.V.: 2013; pp 487-564.
22. VanAtta, R. B.; Strouse, C. E.; Hanson, L. K.; Valentine, J. S., [Peroxotetraphenylporphinato]manganese(III) and [Chlorotetraphenylporphinato]manganese(II) Anions. Synthesis, Crystal Structures, and Electronic Structures. *Journal of the American Chemical Society* **1987,** *109*, 1425-1434.
23. Kitajima, N.; Komatsuzaki, H.; Hikichi, S.; Osawa, M.; Moro-oka, Y., A Monomeric Side-On Peroxo Manganese(III) Complex: $Mn(O_2)(3,5\text{-}iPr_2pzH)(HB(3,5\text{-}iPr_2pz)_3)$. *J. Am. Chem. Soc.* **1994,** *116*, 11596-11597.
24. Singh, U. P.; Sharma, A. K.; Hikichi, S.; Komatsuzaki, H.; Moro-oka, Y.; Akita, M., Hydrogen bonding interaction between imidazolyl N-H group and peroxide: Stabilization of Mn(III)-peroxo complex $Tp^{iPr2}Mn(\eta^2\text{-}O_2)(im^{Me}H)$ ($im^{Me}H$ = 2-methylimidazole). *Inorg. Chim. Acta* **2006,** *359*, 4407-4411.

25. Seo, M. S.; Kim, J. Y.; Annaraj, J.; Kim, Y.; Lee, Y.-M.; Kim, S.-J.; Kim, J.; Nam, W., [Mn(tmc)(O2)]+: A Side-On Peroxido Manganese(III) Complex Bearing a Non-Heme Ligand. *Angew. Chem., Int. Ed.* **2007,** *46* (3), 377-380.
26. Annaraj, J.; Cho, J.; Lee, Y.-M.; Kim, S. Y.; Latifi, R.; de Visser, S. P.; Nam, W., Structural Characterization and Remarkable Axial Ligand Effect on the Nucleophilic Reactivity of a Nonheme Manganese(III)-Peroxo Complex. *Angew. Chem. Int. Ed.* **2009,** *48* (23), 4150-4153.
27. Kang, H.; Cho, J.; Cho, K.-B.; Nomura, T.; Ogura, T.; Nam, W., Mononuclear Manganese–Peroxo and Bis(μ-oxo)dimanganese Complexes Bearing a Common N-Methylated Macrocyclic Ligand. *Chem.--Eur. J.* **2013**, n/a-n/a.
28. Colmer, H. E.; Geiger, R. A.; Leto, D. F.; Wijeratne, G. B.; Day, V. W.; Jackson, T. A., Geometric and electronic structure of a peroxomanganese(iii) complex supported by a scorpionate ligand. *Dalton Trans.* **2014,** *43*, 17949-17963.
29. Coggins, M. K.; Kovacs, J. A., Structural and Spectroscopic Characterization of Metastable Thiolate-Ligated Manganese(III)–Alkylperoxo Species. *J. Am. Chem. Soc.* **2011,** *133* (32), 12470-12473.
30. Coggins, M. K.; Martin-Diaconescu, V.; DeBeer, S.; Kovacs, J. A., Correlation Between Structural, Spectroscopic, and Reactivity Properties Within a Series of Structurally Analogous Metastable Manganese(III)–Alkylperoxo Complexes. *J. Am. Chem. Soc.* **2013,** *135* (11), 4260-4272.
31. Geiger, R. A.; Chattopadhyay, S.; Day, V. W.; Jackson, T. A., A Series of Peroxomanganese(III) Complexes Supported by Tetradentate Aminopyridyl Ligands: Detailed Spectroscopic and Computational Studies. *J. Am. Chem. Soc.* **2010,** *132* (8), 2821-2831.
32. Geiger, R. A.; Chattopadhyay, S.; Day, V. W.; Jackson, T. A., Nucleophilic reactivity of a series of peroxomanganese(III) complexes supported by tetradentate aminopyridyl ligands. *Dalton Trans.* **2011,** *40*, 1707-1715.
33. Geiger, R. A.; Leto, D. F.; Chattopadhyay, S.; Dorlet, P.; Anxolabéhère-Mallart, E.; Jackson, T. A., Geometric and Electronic Structures of Peroxomanganese(III) Complexes Supported by Pentadentate Amino-Pyridine and -Imidazole Ligands. *Inorg. Chem.* **2011,** *50* (20), 10190-10203.
34. Geiger, R. A.; Wijeratne, G.; Day, V. W.; Jackson, T. A., Steric and Electronic Influences on the Structures of Peroxomanganese(III) Complexes Supported by Tetradentate Ligands. *European Journal of Inorganic Chemistry* **2012**, 1598-1608.
35. Leto, D. F.; Chattopadhyay, S.; Day, V. W.; Jackson, T. A., Reaction landscape of a pentadentate N5-ligated MnII complex with O2[radical dot]- and H2O2 includes conversion of a peroxomanganese(iii) adduct to a bis([small mu]-oxo)dimanganese(iii,iv) species. *Dalton Trans.* **2013,** *42* (36), 13014-13025.
36. Borovik, A. S., Bioinspired Hydrogen Bond Motifs in Ligand Design: The Role of Noncovalent Interactions in Metal Ion Mediated Activation of Dioxygen. *Acc. Chem. Res.* **2004,** *38* (1), 54-61.
37. Shook, R. L.; Gunderson, W. A.; Greaves, J.; Ziller, J. W.; Hendrich, M. P.; Borovik, A. S., A Monomeric Mn^{III}-Peroxo Complex Derived Directly from Dioxygen. *J. Am. Chem. Soc.* **2008,** *130* (28), 8888-8889.
38. Shook, R. L.; Peterson, S. M.; Greaves, J.; Moore, C.; Rheingold, A. L.; Borovik, A. S., Catalytic Reduction of Dioxygen to Water with a Monomeric Manganese Complex at Room Temperature. *J. Am. Chem. Soc.* **2011,** *133* (15), 5810-5817.
39. El Ghachtouli, S.; Vincent Ching, H. Y.; Lassalle-Kaiser, B.; Guillot, R.; Leto, D. F.; Chattopadhyay, S.; Jackson, T. A.; Dorlet, P.; Anxolabehere-Mallart, E., Electrochemical formation of MnIII-peroxo complexes supported by pentadentate amino pyridine and imidazole ligands. *Chem. Commun.* **2013,** *49* (50), 5696-5698.
40. Groni, S.; Blain, G.; Guillot, R.; Policar, C.; Anxolabéhère-Mallart, E., Reactivity of Mn^{II} with Superoxide. Evidence for a $[Mn^{III}OO]^{+}$ Unit by Low-Temperature Spectroscopies. *Inorg. Chem.* **2007,** *46* (6), 1951-1953.

41. Groni, S.; Dorlet, P.; Blain, G.; Bourcier, S.; Guillot, R.; Anxolabéhère-Mallart, E., Reactivity of an Aminopyridine $[LMn^{II}]^{2+}$ Complex with H_2O_2. Detection of Intermediates at Low Temperature. *Inorg. Chem.* **2008,** *47* (8), 3166-3172.
42. Sisemore, M. F.; Selke, M.; Burstyn, J. N.; Valentine, J. S., Metalloporphyrin Peroxo Complexes of Iron(III), Manganese(III), and Titanium(IV). Comparative Studies Demonstrating That the Iron(III) Complex Is Extremely Nucleophilic. *Inorganic Chemistry* **1997,** *36* (6), 979-984.
43. Colmer, H. E.; Howcroft, A. W.; Jackson, T. A., Formation, Characterization, and O–O Bond Activation of a Peroxomanganese(III) Complex Supported by a Cross-Clamped Cyclam Ligand. *Inorg. Chem.* **2016,** *55* (5), 2055-2069.
44. Magherusan, A. M.; Zhou, A.; Farquhar, E. R.; García-Melchor, M.; Twamley, B.; Que, L.; McDonald, A. R., Mimicking Class I b Mn2-Ribonucleotide Reductase: A MnII2 Complex and Its Reaction with Superoxide. *Angewandte Chemie International Edition* **2018,** *57* (4), 918-922.
45. Barman, P.; Upadhyay, P.; Faponle, A. S.; Kumar, J.; Nag, S. S.; Kumar, D.; Sastri, C. V.; de Visser, S. P., Deformylation Reaction by a Nonheme Manganese(III)–Peroxo Complex via Initial Hydrogen-Atom Abstraction. *Angewandte Chemie International Edition* **2016,** *55* (37), 11091-11095.
46. Evans, D. F.; Jakubovic, D. A., Water-soluble hexadentate Schiff-base ligands as sequestrating agents for iron(III) and gallium(III). *J. Chem. Soc., Dalton Trans.* **1988,** (12), 2927-2933.
47. Bain, G. A.; Berry, J. F., Diamagnetic Corrections and Pascal's Constants. *Journal of Chemical Education* **2008,** *85* (4), 532.
48. Data Collection: SMART Software in APEX2 v2010.3-0 Suite. Bruker-AXS, E. C. P., Madison, WI 53711-5373 USA.
49. Data Reduction: SAINT Software in APEX2 v2010.3-0 Suite. Bruker-AXS, E. C. P., Madison, WI 53711-5373 USA.
50. International Tables for Crystallography, V. A., 4th ed., Kluwer: Boston (1996).
51. Refinement: SHELXTL v2010.3-0. Bruker-AXS, E. C. P., Madison, WI 53711-5373 USA.
52. Duke, F. R.; Haas, T. W., THE HOMOGENEOUS BASE-CATALYZED DECOMPOSITION OF HYDROGEN PEROXIDE1. *The Journal of Physical Chemistry* **1961,** *65* (2), 304-306.
53. George, G. N. *EXAFSPAK*, Stanford Synchrotron Radiation Laboratory; Stanford, CA, 1990.
54. Ravel, B.; Newville, M., ATHENA, ARTEMIS, HEPHAESTUS: data analysis for X-ray absorption spectroscopy using IFEFFIT. *Journal of Synchrotron Radiation* **2005,** *12* (4), 537-541.
55. Rehr, J. J.; Mustre de Leon, J.; Zabinsky, S. I.; Albers, R. C., Theoretical x-ray absorption fine structure standards. *Journal of the American Chemical Society* **1991,** *113* (14), 5135-5140.
56. Wojdyr, M., Fityk: a general-purpose peak fitting program. *Journal of Applied Crystallography* **2010,** *43* (5 Part 1), 1126-1128.
57. Neese, F., Software update: the ORCA program system, version 4.0. *Wiley Interdisciplinary Reviews: Computational Molecular Science* **2018,** *8* (1), e1327.
58. Becke, A. D., Density-functional Thermochemistry. III. The Role of Exact Exchange. *J. Chem. Phys.* **1993,** *98* (7), 5648-5652.
59. Lee, C.; Yang, W.; Parr, R. G., Development of the Colle-Salvetti Correlation-energy Formula into a Functional of the Electron Density. *Phys. Rev. B* **1988,** *37* (2), 785-789.
60. Grimme, S.; Antony, J.; Ehrlich, S.; Krieg, H., A consistent and accurate ab initio parametrization of density functional dispersion correction (DFT-D) for the 94 elements H-Pu. *The Journal of Chemical Physics* **2010,** *132* (15), 154104.
61. Grimme, S.; Ehrlich, S.; Goerigk, L., Effect of the damping function in dispersion corrected density functional theory. *Journal of Computational Chemistry* **2011,** *32* (7), 1456-1465.
62. Weigend, F., Accurate Coulomb-fitting basis sets for H to Rn. *Physical Chemistry Chemical Physics* **2006,** *8* (9), 1057-1065.

63. Weigend, F.; Ahlrichs, R., Balanced basis sets of split valence, triple zeta valence and quadruple zeta valence quality for H to Rn: Design and assessment of accuracy. *Physical Chemistry Chemical Physics* **2005,** *7* (18), 3297-3305.
64. Marenich, A. V.; Cramer, C. J.; Truhlar, D. G., Universal Solvation Model Based on Solute Electron Density and on a Continuum Model of the Solvent Defined by the Bulk Dielectric Constant and Atomic Surface Tensions. *The Journal of Physical Chemistry B* **2009,** *113* (18), 6378-6396.
65. Hirata, S.; Head-Gordon, M., Time-dependent Density Functional Theory for Radicals: An Improved Description of Excited States with Substantial Double Excitation Character. *Chem. Phys. Lett.* **1999,** *302*, 375-382.
66. Hirata, S.; Head-Gordon, M., Time-dependent Density Functional Theory within the Tamm–Dancoff Approximation. *Chem. Phys. Lett.* **1999,** *314*, 291-299.
67. Lenthe, E. v.; Baerends, E. J.; Snijders, J. G., Relativistic regular two-component Hamiltonians. *Journal of Chemical Physics* **1993,** *99* (6), 4597-4610.
68. van Wüllen, C., Molecular density functional calculations in the regular relativistic approximation: Method, application to coinage metal diatomics, hydrides, fluorides and chlorides, and comparison with first-order relativistic calculations. *Journal of Chemical Physics* **1998,** *109* (2), 392-399.
69. Roemelt, M.; Beckwith, M. A.; Duboc, C.; Collomb, M. N.; Neese, F.; DeBeer, S., Manganese K-edge X-ray absorption spectroscopy as a probe of the metal-ligand interactions in coordination compounds. *Inorg Chem* **2012,** *51* (1), 680-7.
70. Surry, D. S.; Buchwald, S. L., Dialkylbiaryl phosphines in Pd-catalyzed amination: a user's guide. *Chem. Sci.* **2011,** *2* (1), 27-50.
71. Childers, W. E.; Havran, L. M.; Asselin, M.; Bicksler, J. J.; Chong, D. C.; Grosu, G. T.; Shen, Z.; Abou-Gharbia, M. A.; Bach, A. C.; Harrison, B. L.; Kagan, N.; Kleintop, T.; Magolda, R.; Marathias, V.; Robichaud, A. J.; Sabb, A. L.; Zhang, M.-Y.; Andree, T. H.; Aschmies, S. H.; Beyer, C.; Comery, T. A.; Day, M.; Grauer, S. M.; Hughes, Z. A.; Rosenzweig-Lipson, S.; Platt, B.; Pulicicchio, C.; Smith, D. E.; Sukoff-Rizzo, S. J.; Sullivan, K. M.; Adedoyin, A.; Huselton, C.; Hirst, W. D., The Synthesis and Biological Evaluation of Quinolyl-piperazinyl Piperidines as Potent Serotonin 5-HT1A Antagonists. *J. Med. Chem.* **2010,** *53* (10), 4066-4084.
72. Ruiz-Castillo, P.; Buchwald, S. L., Applications of Palladium-Catalyzed C–N Cross-Coupling Reactions. *Chemical Reviews* **2016,** *116* (19), 12564-12649.
73. Leto, D. F.; Ingram, R.; Day, V. W.; Jackson, T. A., Spectroscopic properties and reactivity of a mononuclear oxomanganese(iv) complex. *Chem. Commun.* **2013,** *49* (47), 5378-5380.
74. These calculated extinction coefficients assume 100% conversion of the MnII species.
75. Shook, R. L.; Borovik, A. S., Role of the Secondary Coordination Sphere in Metal-Mediated Dioxygen Activation. *Inorganic Chemistry* **2010,** *49* (8), 3646-3660.
76. Bencini, A.; Gatteschi, D., Inorganic Electronic Structure and Spectroscopy. In *Inorganic Electronic Structure and Spectroscopy*, Solomon, E. I.; Lever, A. B. P., Eds. John Wiley & Sons, Inc.: 2006; Vol. Volume I: Methodology, pp 93-155.
77. Leto, D. F.; Jackson, T. A., Mn K-Edge X-ray Absorption Studies of Oxo- and Hydroxo-manganese(IV) Complexes: Experimental and Theoretical Insights into Pre-Edge Properties. *Inorg. Chem.* **2014,** *53* (12), 6179-6194.
78. So, H.; Park, Y. J.; Cho, K.-B.; Lee, Y.-M.; Seo, M. S.; Cho, J.; Sarangi, R.; Nam, W., Spectroscopic Characterization and Reactivity Studies of a Mononuclear Nonheme Mn(III)–Hydroperoxo Complex. *Journal of the American Chemical Society* **2014,** *136* (35), 12229-12232.
79. Ure, A. D.; McDonald, A. R., Nucleophilic Reactivity of a Metal-Bound Superoxide Ligand. *Synlett* **2015,** *26* (15), 2060-2066.
80. Babcock, G. T. In *The oxygen-evolving complex in photosystem II as a metallo-radical enzyme*, Kluwer: 1995; pp 209-215.

81. Pecoraro, V. L.; Baldwin, M. J.; Gelasco, A., Interaction of Manganese with Dioxygen and Its Reduced Derivatives. *Chem. Rev.* **1994,** *94* (3), 807-826.
82. Goldsmith, C. R.; Cole, A. P.; Stack, T. D. P., C−H Activation by a Mononuclear Manganese(III) Hydroxide Complex: Synthesis and Characterization of a Manganese-Lipoxygenase Mimic? *J. Am. Chem. Soc.* **2005,** *127* (27), 9904-9912.
83. Wijeratne, G. B.; Corzine, B.; Day, V. W.; Jackson, T. A., Saturation Kinetics in Phenolic O–H Bond Oxidation by a Mononuclear Mn(III)–OH Complex Derived from Dioxygen. *Inorg. Chem.* **2014,** *53* (14), 7622-7634.
84. Wijeratne, G. B.; Day, V. W.; Jackson, T. A., O-H bond oxidation by a monomeric MnIII-OMe complex. *Dalton Trans.* **2015,** *44* (7), 3295-3306.
85. Coggins, M. K.; Sun, X.; Kwak, Y.; Solomon, E. I.; Rybak-Akimova, E.; Kovacs, J. A., Characterization of Metastable Intermediates Formed in the Reaction between a Mn(II) Complex and Dioxygen, Including a Crystallographic Structure of a Binuclear Mn(III)–Peroxo Species. *J. Am. Chem. Soc.* **2013,** *135* (15), 5631-5640.
86. Sankaralingam, M.; Lee, Y.-M.; Jeon, S. H.; Seo, M. S.; Cho, K.-B.; Nam, W., A mononuclear manganese(iii)-hydroperoxo complex: synthesis by activating dioxygen and reactivity in electrophilic and nucleophilic reactions. *Chemical Communications* **2018,** *54* (10), 1209-1212.
87. Y. N. Ho, R.; Que Jr, L.; Roelfes, G.; L. Feringa, B.; Hermant, R.; Hage, R., Resonance Raman evidence for the interconversion between an [FeIII–η1-OOH] 2+ and [FeIII–η2-O2]+ species and mechanistic implications thereof. *Chemical Communications* **1999,** (21), 2161-2162.
88. Cho, J.; Jeon, S.; Wilson, S. A.; Liu, L. V.; Kang, E. A.; Braymer, J. J.; Lim, M. H.; Hedman, B.; Hodgson, K. O.; Valentine, J. S.; Solomon, E. I.; Nam, W., Structure and reactivity of a mononuclear non-haem iron(III)–peroxo complex. *Nature* **2011,** *478*, 502.

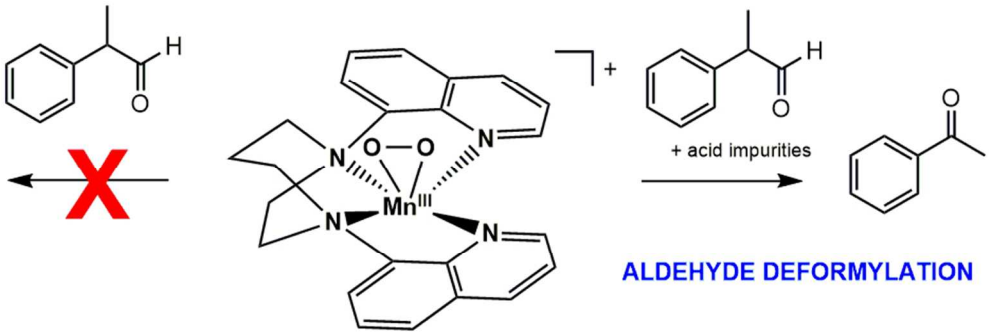

79x27mm (300 x 300 DPI)